Productivity-oriented SLM process parameters effect on the fatigue strength of Inconel 718

G. Macoretta[a*], L. Bertini[a], B.D. Monelli[a], F. Berto[b]

[a] Department of Civil and Industrial Engineering, University of Pisa, Largo Lucio Lazzarino 2, 56126 Pisa, Italy

[b] Department of Chemical Engineering Materials Environment, Sapienza University of Rome, Via Eudossiana 18, 00184 Roma, Italy

* giuseppe.macoretta@ing.unipi.it

Abstract

The low productivity of the SLM process is known to be a limiting factor, but speeding up the process can lead to material defects. Two sets of SLM process parameters enhancing its productivity by 50% were devised and tested in comparison with baseline sets, in terms of material microstructure, porosity, surface roughness, static mechanical properties, and HCF behavior, in the as-built and aged conditions. The as-built surface was investigated. Despite a significant increase in the porosity and surface roughness, the fatigue strength was reduced by 4%. The Murakami $\sqrt{area_R}$ parameter effectively correlates the fatigue strength and surface roughness variations.

Keywords: Selective Laser Melting, S-N curves, High cycle fatigue, Surface roughness, Defects

1. Introduction

Selective Laser Melting (SLM) of metallic materials is emerging as a technology suitable for the industrial production of critical components. The possibility to manufacture complex geometries, the minimization of the design-to-production lead time, and the scarp reduction are some of the key advantages of the technology.

The productivity rate of the SLM process is a limiting factor for the industrial spread of the technology; however, increasing productivity can lead to process instabilities that can jeopardize the mechanical properties of the component, particularly in fatigue strength. SLM machine manufacturers overcame this issue by introducing additional laser beams within the same machine, with the drawback of laser interactions and uniformity issues. However, recent SLM machines featuring a higher laser power, typically 500W, allow exploiting process parameters specifically devised to increase process build rate, with a significant cost reduction.

The SLM process parameters (laser power, scan speed, layer thickness, hatch distance, pre-heating temperature, scanning strategy) and the subsequent heat treatment (stress relieving and aging) play a fundamental role in the fatigue performances of the component, [1–4]. However, the entanglement among the multi-scale and intrinsically unstable phenomena typical of the SLM process makes a process parameters optimization procedure, based on the component's surface finish and strength requirements, still an open issue, [5–10]. The present work aims to contribute to the understanding of the effects on the static and fatigue response of process parameters which significantly enhance SLM productivity.

Nomenclature

AM	Additive Manufacturing		P	laser power
BD	SLM build direction		P^*	normalized laser power
FE	Finite Element		p	pitch between roughness valleys
HCF	High Cycle Fatigue		R	stress ratio
OM	Optical Microscope		Ra	profile arithmetical mean deviation
SEM	Scanning Electron Microscope		Rz	maximum height of the profile
SLM	Selective Laser Melting		$\bar{R}$	minimum meltpool radius
$\sqrt{area_R}$	Murakami roughness parameter		r	predicted meltpool radius
%EL	percent elongation		S_u	ultimate strength
A0, A1, A2	set of process parameters		S_y	yield strength
A_r	meltpool aspect ratio		σ	variance of log(N) normal distribution
Ax	general name of A0, A1, A2 sets		σ_a	stress amplitude
α	thermal diffusivity		σ_e	experimental fatigue strength
B_R	SLM build rate		σ_w	predicted fatigue strength
γ	material mean stress sensitivity		T	temperature
E_d	energy density		$T_{\Delta\sigma}$	scatter parameter
h	hatch distance		T_m	melting temperature
k	thermal conductivity		T_0	reference temperature
k_t	stress concentration factor		t	layer thickness
m	S-N curve slope		UE	uniform elongation
l	meltpool length		V^*	normalized scan velocity
λ	laser absorptivity		v	laser scan velocity

Two sets of productivity-oriented process parameters were defined on the basis of the analytical model proposed by Moda, [11,12], which allows defining a process feasible region through first-order correlations between the process parameters and the boundaries describing the occurrence of the principal defects characterizing the SLM technology, namely lack of fusion or meltpool instability, [13] The proposed set enhanced the SLM build rate by 30 to 50% while preserving a safety margin on the feasible region boundaries.

Local defects caused by the SLM technology are well known to be the governing factors of the material fatigue strength, namely lack of fusion, pores, and hot tearing cracks caused by the thermally induced residual stresses, [14–16]. Furthermore, exploiting the potential of the AM means creating complex-shaped components that are not subjected to further machining processes, at least on the non-mating surfaces or on the internal ones. It is thus crucial to assess the fatigue behavior of specimens featuring the poor as-built surface finish, characterized by irregular profile valleys and surface defects. The behavior of materials containing defects has been explained by Murakami, who showed that the fatigue limit is the threshold stress for non-propagation of the small cracks emanating from the initial defects, [17–19]. This approach has been successfully extended to local defects introduced by SLM, [15,16,20–23]. However, when dealing with surface roughness, the interaction between profile valleys could play a significant role in reducing the stress

concentration caused by a single valley. As pointed out by the work of Murakami, [17,24], the surface roughness effects can be analyzed by considering the roughness valleys as periodic cracks, in terms of the $\sqrt{area_R}$ parameter, which includes the effects of the height and pitch of the roughness valleys, [17].

In the present work, the static mechanical properties and the HCF behavior of Inconel 718 cylindrical specimens printed by employing four sets of SLM process parameters, a standard set and three productivity-oriented ones, were investigated in the as-built and aged material condition, and as-built surface condition. A FE model, including the effective specimen profile, was set up to investigate the stress concentration effects produced by the surface irregularities. The fatigue strength was finally correlated with the surface roughness through the approach developed by Murakami, obtaining an effective correlation between the fatigue strength variation and the $\sqrt{area_R}$ parameter.

2. Material and Methods

2.1. SLM process parameters selection

The thermal field produced by the laser beam acting on a flat surface can be modeled by considering the solution for a steady-state point heat source moving along a straight line with constant velocity on the flat surface of a semi-infinite solid with constant thermophysical properties, typically called ''Rosenthal solution'', [25–28]. Within this framework, the work of Moda, [11,12], extended the Rosenthal solution to modeling the thermal field produced by the SLM process and successfully defined a material-independent process feasible region, depending only on the principal process parameters characterizing the SLM process (laser power, scan speed, layer thickness, hatch distance, substrate temperature) and the material thermal properties. It represents a first-order approximation, which neglects the effects of non-constant thermal properties, actual heat distribution, boundary effects, and convective phenomena occurring in the meltpool region, but provides an analytical formulation catching the macroscopic effects of the SLM process, [13]. Considering an Eulerian reference frame centered on the point heat source, the thermal field can be written as:

$$T(x, y, z) = T_0 + \frac{P}{2 \pi k r \lambda} \cdot exp\left(-\frac{v}{2 \alpha}\left(\sqrt{x^2 + y^2 + z^2} + x\right)\right) \tag{1}$$

where P is the laser power, λ the laser absorptivity (in general dependent on the powder chemical composition and grain size distribution), v the scan velocity, α and k the thermal diffusivity and conductivity of the solidified substrate, x, y and z the distance from the point heat source along the coordinate axes, Fig. 1, and T_0 the reference temperature far from the heat source. If we consider the perimeter of the melting temperature (T_m) isotherm surface as the boundary of the meltpool, which is moving along a straight line at the scan laser velocity, a prediction of the meltpool geometry can be obtained, [12], as shown in Fig. 1. The meltpool radius (r), length (l), and aspect ratio (A_r) can be thus evaluated as:

$$r \approx \frac{P}{2 \pi k \lambda (T_m - T_0)}\left[1 + \left(\frac{8 \pi \lambda k \alpha (T_m - T_0)}{e p v}\right)^{\beta/2}\right]^{1/\beta} \tag{2}$$

$$A_r = \frac{l}{2 \cdot r} \approx \left[1 + \left(\frac{e}{32 \, \pi} \, \frac{P \, v}{\alpha \, k \, \lambda \, (T_m - T_0)} \right)^{n/2} \right]^{1/n} \tag{3}$$

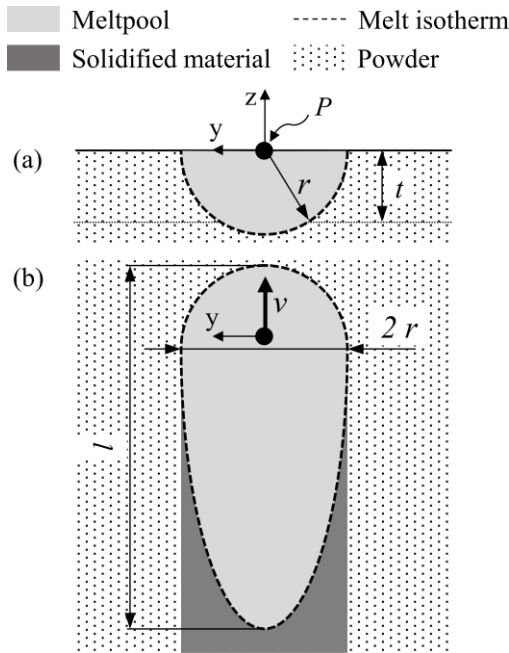where n and β are numerically evaluated constants, [27].

Fig. 1. Cross-section at the maximum width (a) and top view (b) of the meltpool predicted for a single scan line.

The minimum meltpool radius ($\bar{R}$), necessary to avoid the formation of lack of fusion areas between adjacent scan lines or layers, can be defined on the basis of the hatch distance (h) and layer thickness (t):

$$\bar{R} = \sqrt{\frac{h^2}{4} + t^2} \tag{4}$$

The four principal process parameters, namely laser power, scan velocity, hatch distance and layer thickness, can be thus condensed into two dimensionless parameters, named "normalized velocity" (V^*) and "normalized power" (P^*):

$$V^* = \frac{v \, \bar{R}}{2 \, \alpha} \tag{5}$$

$$P^* = \frac{P}{2 \, \pi \, k \, \lambda \, \bar{R}(T_m - T_0)} \tag{6}$$

Once the material thermal properties near the solidus temperature [29], and the material laser absorptivity, λ, for a laser beam having the same characteristic length as the one employed on the SLM machine [30,31] are known, the model allows for defining an SLM feasibility region, namely a set of combinations of P^* and V^* that lead to a nominally full-dense material. The SLM feasibility region for the Inconel 718 alloy is represented in Fig. 2 by the grey hatched area. It is lower bounded by the lack of fusion curve, where the predicted radius, r, is equal to the minimum value, $\bar{R}$. The dashed lines in Fig. 2 represent meltpool having the same A_r, which is known to be linked to SLM process instability (i.e., humping) and hot tearing cracks, [2,32,33]. The keyhole region was extrapolated from literature data.

Two sets of literature process parameters were considered as a benchmark: a standard set, named "*baseline,* containing

the values suggested by Renishaw for the RenAM500E SLM machine (similar, in terms of P^* and V^*, to the parameters suggested by other manufacturers, i.e. [6,34]); a productivity-oriented one, adapted from [9] and named "$A0$".

Neglecting the fixed dwell time due to the recoater motion, the productivity of the SLM process can be evaluated in terms of the nominal melted volume per unit of time, namely the process build rate (B_R):

$$B_R = t \cdot h \cdot v \tag{7}$$

If we assume to preserve the vertical resolution of the printing process, namely keeping a constant layer thickness, the gain in productivity can be obtained by increasing the scan velocity and the hatch distance. The predicted SLM feasible region was thus employed to develop two sets of productivity-oriented process parameters, named "$A1$" and "$A2$", that present a higher B_R while complying with the lack of fusion and keyhole boundaries, as shown in Fig. 2. A 20% safety margin to the occurrence of lack of fusion phenomena, expressed as the ratio between the predicted meltpool radius and the $\bar{R}$ value, was imposed. The $A1$ and $A2$ sets feature a higher A_r than the sets adopted in the recent literature, respectively 8 and 10, against a standard of 5. As listed in Table 1, compared to the *baseline* case, the process productivity is increased by 60%, 110%, and 120% for the A0, A1, and A2 sets, respectively.

The adopted process parameters are listed in Table 1, along with the corresponding A_r and energy density (E_d), which is defined as:

$$E_d = \frac{P}{v\,h\,t} \tag{8}$$

For the sake of brevity, the "$A0$", "$A1$", and "$A2$" sets are named "Ax" when a common feature is described.
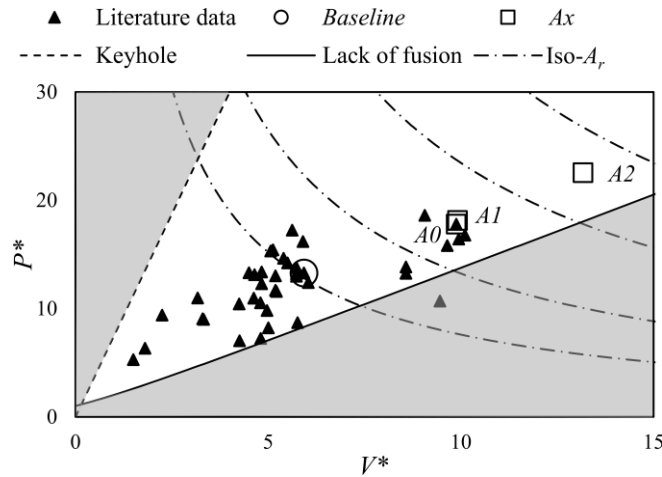

Fig. 2. Selected process parameters within the SLM feasible region for the alloy Inconel 718. Literature data from [12].

	P	v	h	t	A_r	E_d	B_R	
	W	m/s	μm	μm	-	J/mm^3	mm^3/s	Δ
Baseline	280	0.9	90	60	5	57.6	4.9	-
A0	380	1.45	90	60	8	48.5	7.8	+61%
A1	460	1.25	135	60	8	45.4	10.1	+108%
A2	475	2	90	60	10	44.0	10.8	+122%

Table 1. SLM process parameters, along with the corresponding meltpool aspect ratio (A_r) and process build rate (B_R).

2.2. Specimen production

A standard Inconel 718 powder, provided by Heraeus Electro-Nite GmbH & Co. KG (Hanau, Germany), featuring a chemical composition compliant with the ASTM F3055 standard, produced by Vacuum Inert Gas Atomization (VIGA), and featuring a Particle Size Distribution (PSD) comprised within the range 13 μm ÷ 53 μm (D10 ÷ D90) was employed. Specimens were produced using a Renishaw RenAM 500E SLM machine, characterized by a maximum laser power of 500W, installed in the "Metal Additive Manufacturing" laboratory of the University of Pisa. The laser beam modulation parameters were set to have a continuous wave emission.

Cylindrical specimens were built in a vertical direction, namely with the longitudinal direction aligned with the direction of motion of the built plate. Apart from the *baseline* case, which employs the standard Renishaw contour strategy, the parameters reported in Table 1 were adopted for both hatching and contour regions. A stripe scanning strategy and a layer rotation of 67° were employed for the hatching region, while a standard contour scanning path was used for the outer region. All the specimens were printed within a unique batch, where the build plate was heated at 170°C, to minimize the residual stresses, and the process chamber was filled with gas argon, reaching an oxygen concentration lower than 7 ppmw, which guarantees to avoid oxidation phenomena. No distortion was found in the specimens after removal from the built plate.

Specimens produced by using the *baseline* and *A2* sets were subjected to the aging heat treatment. It was used a Nabertherm LH/120 furnace, featuring a protective gas box, continuously flushed with gas argon to prevent oxidation, and a controlled cooling apparatus. In agreement with the AMS 5663 standard and the literature data, [35], the heat treatment is composed of solution treatment (980 °C, 1 h followed by a furnace forced cooling to 50°C) and a double aging (720 °C, 8 h; furnace cooling at 55 °C/h to 620 °C; 8 h/air cooling).

2.3. Static mechanical tests

Tensile tests were carried out at room temperature on an MTS servo-hydraulic machine having a load capacity of 50 kN, equipped with an extensometer featuring a gauge length of 10 mm (MTS 634.21-F25). The tests were done with displacement control of 0.005 mm/s, corresponding to a strain rate of about $1 \cdot 10^{-4}$ s^{-1}. A round specimen was employed, designed in compliance with the ASTM E8-16 standard and having a gauge diameter of 6 mm. To investigate the SLM process repeatability, at least 3 specimens, printed in various locations on the build plate, were tested for each set. The specimens were tested in the as-built surface condition. The specimen's dimensions are reported in Fig. 3 (a).

Vickers hardness measurements were carried out on polished samples extracted in the transverse direction from the gauge length of untested specimens, employing a Mitutoyo AVK-C1 hardness tester and imposing a load of 10kg and a loading time of 10s. Hardness was measured both in the inner and outer regions of the specimen, keeping a distance of at least 2.5 and 3 times the indentation diagonal from the specimen contour and adjacent measurements, respectively, in

agreement with the ISO 6507 standard.

2.4. Fatigue tests

HCF tests were carried out at room temperature in an axial loading configuration on a RUMUL Mikrotron resonant testing machine, with a load ratio (R) of 0.05. In the case of the "*baseline*" set, in the as-built material condition, load ratios of 0.4 and -1 were investigated as well. The test frequency was monitored to detect the macroscopic crack propagation phase by exploiting the consequent specimen stiffness reduction. Specimens were tested in the surface as-built condition.

A round specimen was adopted, designed in compliance with the ASTM E466 standard and featuring a uniform diameter along the gauge length, Fig. 3 (b). It allows having a wide iso-stressed region exposed to the surface and microstructural defects, and thus maximizes their effects on the fatigue response. The load applied to each specimen was defined based on the effective gauge dimension. The measurement uncertainty was ± 0.01 mm, which, combined with the load cell accuracy, leads to a maximum error of 1% on the applied stress.

The fatigue data obtained were presented in S-N diagrams, along with fitting lines corresponding to a 50% probability of failure, scatter bands at 97.5 and 2.5 probability of failure with a confidence level of 90%, [36], and confidence bands calculated in compliance with the ASTM E739 and ISO 12107 standards. The scatter index of the S-N curves, $T_{\Delta\sigma}$, was defined as:

$$\frac{1}{T_{\Delta\sigma}} = \frac{\Delta\sigma_{Ps=10\%}}{\Delta\sigma_{Ps=90\%}} = 10^{\frac{2k\sigma}{m}} \tag{9}$$

where k is the coefficient of the one-sided tolerance limit corresponding to a 97.5% probability of failure and a 0.9 confidence level, σ is the standard deviation of the logarithmic fatigue life (normally distributed), and m is the inverse slope of the fitting line. The fatigue strength was defined as the value calculated from the S-N fitting line at 1 million cycles to failure, and, unless otherwise specified, it refers to the stress amplitude value (σ_a).
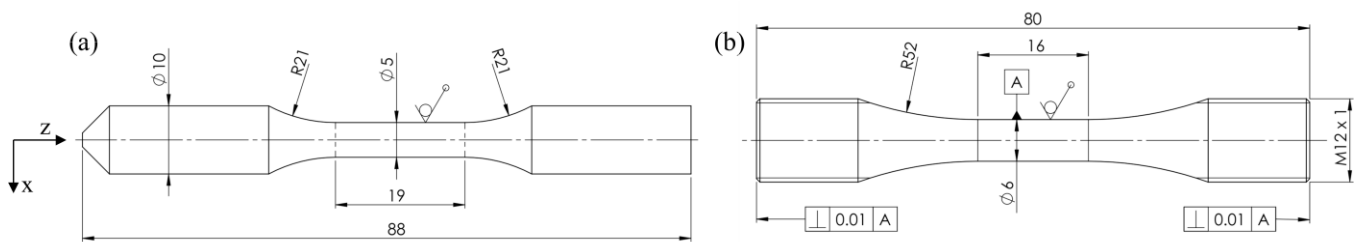

Fig. 3. Specimen employed in the tensile (a) and HCF (b) tests. Dimensions in millimeters.

2.5. Microstructural and fractographical analysis

Microstructural investigations were carried out both in longitudinal and transverse directions. Specimens were prepared following the ASTM E3-11 standard and were etched with Kalling's II (n.94, ASTM E407) and Lucas's reagent, [37]. Specimen porosity was investigated by Optical Microscope (OM) through sections extracted both in the specimen longitudinal and transversal directions, namely parallel or orthogonal to the building direction. The material density and

the pore size and shape distribution were measured using the software ImageJ, [38]. At least 20 sections extracted from the gauge length of different specimens were investigated per each process parameters set.

Fractographic investigations were carried out by stereo-microscope and Scanning Electron Microscope (SEM), FEI Quanta 450 FEG-SEM equipped with an EDX spectrometer Bruker QUANTAX XFlash Detector 6|10. The same samples were successively analyzed through metallographic inspections, with sections parallel to the specimen's longitudinal (z) direction, to observe the crack propagation path and investigate the presence of non-propagating cracks within its gauge length.

2.6. Surface roughness measurement and analysis

The surface roughness was measured in the specimen's longitudinal direction by extracting the specimen profile from metallographic sections, Fig. 4 (a), to observe in detail the surface irregularities near the valley apex. It was considered the angular position corresponding to the plane containing the fatigue crack onset. Samples were prepared as in the case of the microstructural analyses and examined by OM with a 10x magnification factor. The images were thus elaborated using the software ImageJ, as shown in Fig. 4 (a) and (b). A Matlab® routine was developed to calculate the roughness values according to the ISO standard 4287:1998. As the length of the sampled profiles was equal to 0.8 mm and they were extracted only from the specimen gauge length, it can be assumed that the contribution due to longwave components of the specimen profile is rejected. About 50 sampling lengths per process parameters set were considered.

To validate this strategy, the surface roughness in the specimens' longitudinal direction was preliminarily measured by a profilometer, Jenoptik Waveline W812R, using a stylus having a tip radius of 2 μm. To reject the spurious roughness due to powder particles partially bonded to the surface, roughness profiles were measured in eight angular positions for each specimen, spaced by 45°. The average value among the six smoother profiles was considered. The sampling length was defined according to the ISO standard 4288:1998.

The extracted profile was also employed to set up an FE model featuring the actual specimen surface profile. Under the hypothesis of a uniform profile in the specimen hoop direction, a 2D axisymmetric model was set up, imposing a uniform tensile pressure, and on the opposite side a null axial displacement, at a distance greater than 5 times the specimen diameter from the investigated region, Fig. 4 (c). High-order 2D 6-nodes triangular elements were employed in the outer region, Fig. 5 (d), whose minimum size had been defined through a mesh convergence analysis. The peak stress reaches a plateau region for an element size of 0.002 mm, resulting in about 2 million DOFs, Fig. 4 (e). A coarser mesh, based on high-order 2D 8-nodes quadrilateral elements, was employed for the inner region. For both regions, a pure displacement formulation was employed. A homogeneous, isotropic, stress-free, and linear elastic material was assumed. Young's modulus was obtained from the tensile tests of the *baseline* case, while a value of 0.294 was assumed for the Poisson's ratio [39,40]. Ten profiles were examined per each process parameters set. The model was solved in Ansys Mechanical®.
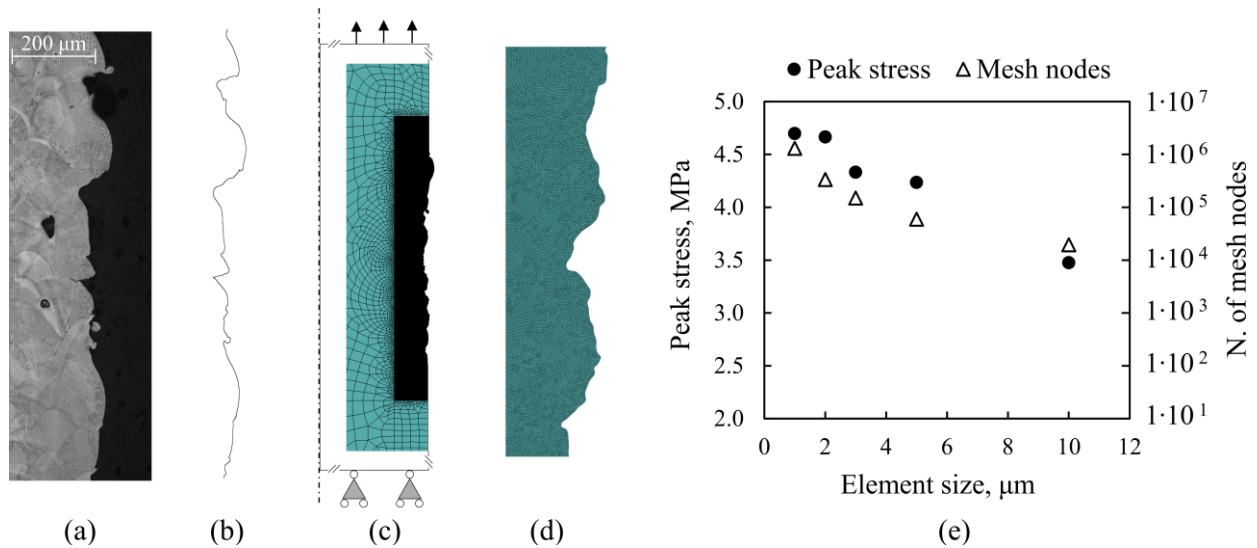
Fig. 4. Surface roughness measurement and analysis. Specimen profile (a) extracted profile (b), FE model presentation (c), detail of the mesh employed in the outer region (d), and mesh convergence analysis (e).

3. Results and Discussion

3.1. Porosity and microstructural analysis

The *baseline* set resulted to produce an almost full-dense material, having a density of 99.95%, examined both from sections extracted in the longitudinal and transverse direction, due to the presence of some sporadic pore. A significant increase in the dimension and frequency of the pores was observed for the *Ax* process parameters, as shown in the sections reported in Fig. 5, leading to a density of 99.7% in the worst case. In Table 2, the resulting material density is reported along with the observed pore area and the pore aspect ratio, defined as the ratio of the major and minor axes of the particle's fitted ellipse. The reported pore area and aspect ratio are the average values calculated among the first 5 largest pores of each set.

Some sporadic pores were present in the *baseline* case, but they are small (diameter less than 50 μm) and round, suggesting that they arise from entrapped gas bubbles. On the other side, the pores present in the *A1* and *A2* cases are significantly larger and more elongated. As the pores are sparse and rare, the material density is not significantly affected, but they can cause a significant stress concentration. These larger pores are caused by local instabilities of the meltpool, which create local lack of fusion areas or cavities. Due to meltpool perturbation arising from the high velocity and aspect ratio, some portion of the meltpool region can solidify without being open to the molten material pool. Smaller pores are frequent in proximity to the specimen surface, in particular in the *A2* case, suggesting that a key role was played by the process parameters adopted for the specimen contours. The adoption of specific contour parameters could minimize this problem.

	Baseline		A0		A1		A2	
Section plane	L	T	L	T	L	T	L	T
Density, %	99.97 ± 0.02	99.95 ± 0.03	99.90 ± 0.04	99.89 ± 0.03	99.84 ± 0.1	99.79 ± 0.05	99.71 ± 0.1	99.88 ± 0.07
Pore area, μm^2	800 ± 200	1450 ± 500	1500 ± 600	1450 ± 500	3700 ± 800	2200 ± 700	3400 ± 800	1800 ± 700
Pore aspect ratio	1.3 ± 0.3	1.2 ± 0.2	1.8 ± 0.6	1.6 ± 0.5	2.0 ± 0.6	2.1 ± 0.4	2.3 ± 0.8	2.0 ± 0.7

Table 2. Results of the porosity analysis on longitudinal (L) and transversal (T) sections, reported as mean value ± standard deviation.
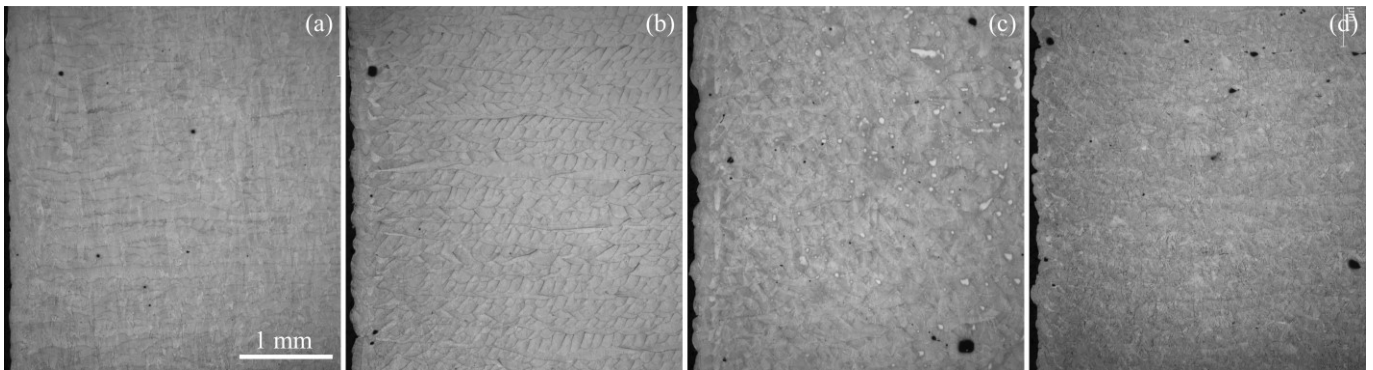
Fig. 5. Metallographic examinations in longitudinal direction: (a) *baseline*, (b) *A0*, (c) *A1*, (d) *A2* process parameters set.

The microstructural analysis showed that the four sets of process parameters are pretty similar in terms of meltpool geometries and grain shapes, Fig. 6 (a-b). As typical for a material produced by SLM, [41], segregation of micro-precipitates can be observed near the meltpool edges, revealing that, as predicted by the analytical model, the meltpool dimension of the *baseline* and *Ax* are similar. Columnar structures oriented along the build direction, parallel to the solidification thermal gradient, and extending for several layers can be observed in both cases. Within the columnar structures, regions characterized by small cuboidal particles of γ''(Ni₃Nb), in solid solution in the γ matrix, and fine columnar dendrites, typical of fast cooling rates [41], can be observed as well. The principal difference between the *baseline* and the *Ax* cases was found to be the presence of larger gas-entrapped pores and lack of fusion regions due to local meltpool instabilities, Fig. 6 (c), which, nonetheless, does not affect the material features in the surrounding region.
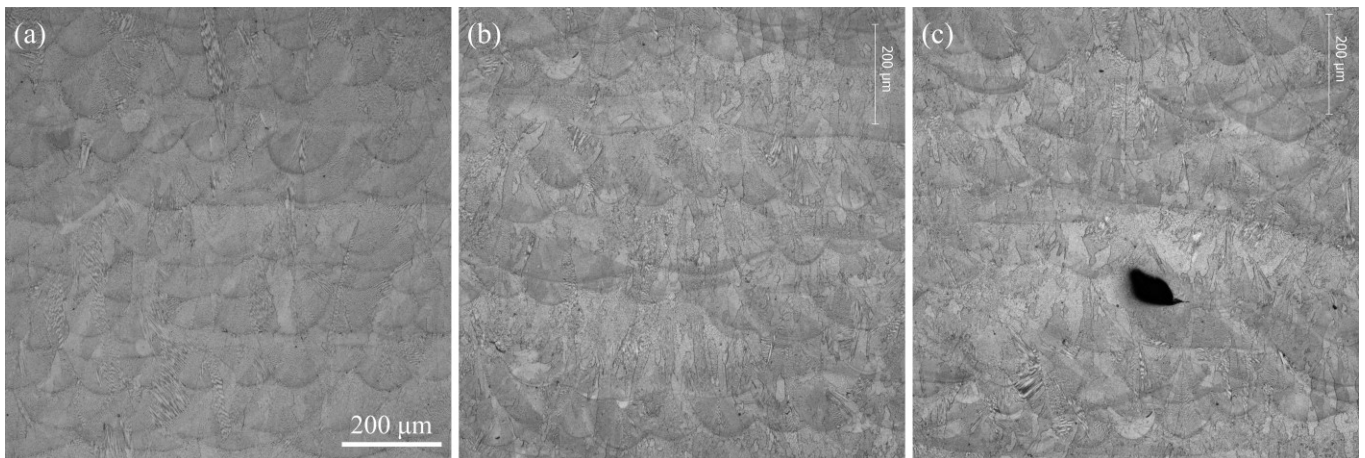

Fig. 6. Longitudinal sections observed by OM revealing the material microstructure, as-built condition: *baseline* (a) and *A2* (b and c) sets. Kalling's II etchant

3.2. Surface roughness

For all the tested sets, the surface roughness values obtained by the extraction of the specimen profile were found to be aligned with the profilometer measurements, with the former being constantly greater. The relative difference is proportional to the roughness height, confirming the effectivity of the method in the presence of steep and irregular valleys. Table 3 reports the values of the arithmetical mean deviation of the assessed profile (Ra), the maximum height of the profile within a sampling length (Rz), the largest profile valley depth (Rv), and the root mean square value of the ordinate slopes ($R\Delta q$) measured by the profile investigation. The Ax sets markedly increase the surface roughness, both in terms of average and total height of the roughness profile, which are more than doubled compared to the *baseline* case. The measured values are in line with the values reported in the literature for as-built surfaces, [42].

In Fig. 7, the most irregular profile observed in the *baseline* case is compared to typical profiles observed in the *Ax* cases. The *Ax* sets cause a strong irregularity of the roughness profile, which becomes markedly jagged, featuring deep and steep valleys. The presented sections were etched to reveal the meltpool boundaries and the traces of the SLM process. In the case of the *A0* set, the surface undulation arises from irregularities in the meltpool dimensions, while in the *A1* and *A2* sets it appears that the meltpool itself is less regular due to the increased A_r, leading to steeper valleys.

The pitch among two consecutive roughness valleys, measured from the extracted profile, was found to be strongly affected by the SLM process parameters sets, Fig. 8. For the baseline condition, values comprised between 180 μm and 780 μm, namely 3 to 13 times the layer thickness, are evenly distributed, with a maximum frequency near 480 μm, as shown in Fig. 8 (a). In the *Ax* cases, the specimen profile features a superposition of two patterns, one featuring deeper valleys at a longer pitch and one with many shallow and less steep valleys at a finer pitch, which characterizes the jagged surface profile, Fig. 8 (b-d). The more frequent value, governed by the shallow irregularities, is comprised in the range between 180 μm and 360 μm, namely 3 to 6 times the adopted layer thickness.

	Baseline	**A0**	**A1**	**A2**
Ra, μm	7 ± 2	13 ± 3	17 ± 4	19 ± 3
Rz, μm	42 ± 9	73 ± 20	91 ± 26	95 ± 20
Rv, μm	19 ± 5	38 ± 11	49 ± 19	47 ± 13
R\Delta q	0.32 ± 0.03	0.42 ± 0.04	0.41 ± 0.04	0.48 ± 0.05

Table 3. Surface roughness parameters, reported in terms of mean value ± standard deviation.
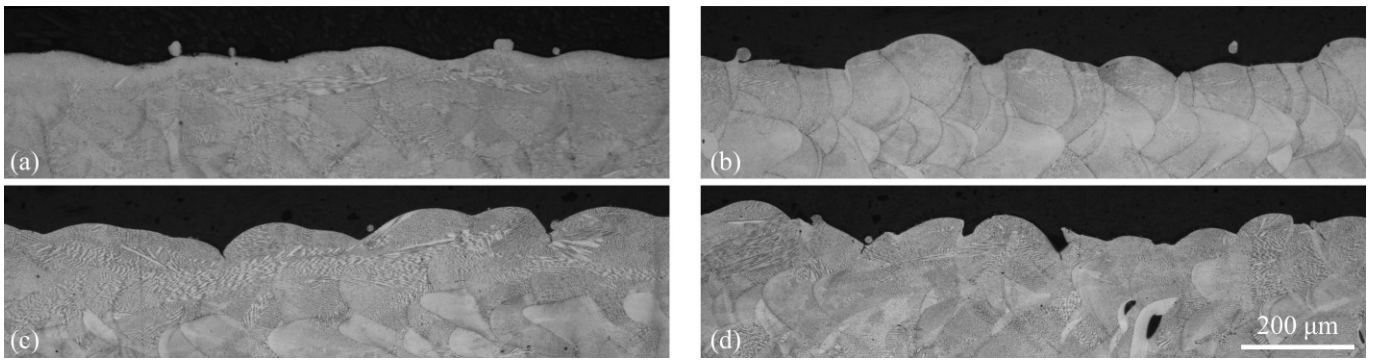
Fig. 7. Surface roughness profiles: *baseline* (a), *A0* (b), *A1* (c), and *A2* (d) process parameters set. For the *baseline* case, it was reported the worst case among the observed profiles, while typical patterns are reported for *Ax* cases.
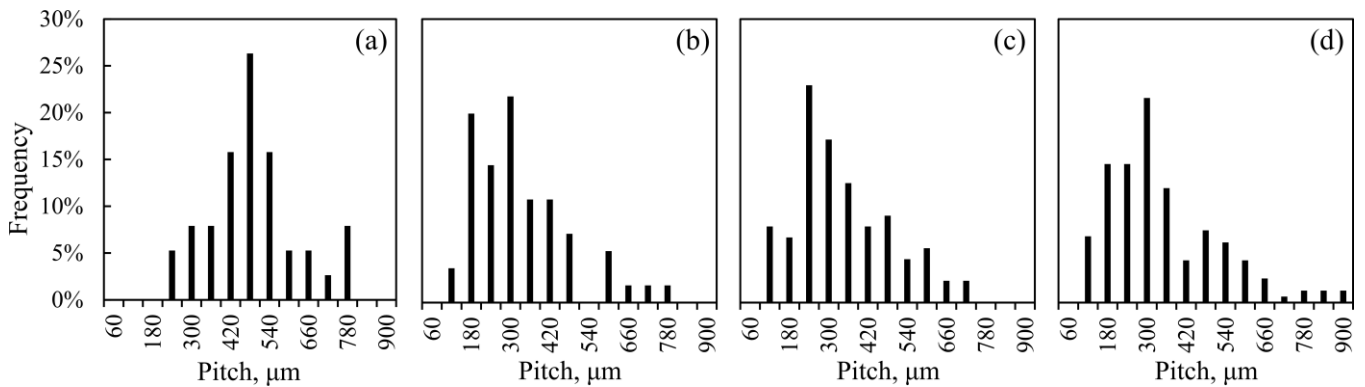

Fig. 8. Histogram of pitch between consecutive valleys of the roughness profile: (a) *baseline*, (b) *A0*, (c) *A1*, (d) *A2* cases.

3.3. Static tests

The investigated sets were found to affect the tensile behavior mainly in terms of elongation at fracture (%EL), which is markedly lower for the *Ax* sets, while the yield and ultimate strength were found to be slightly increased, as shown in Fig. 9 (a) and Table 4. The process parameters impact the necking and post-necking phases. While the uniform elongation (UE), namely the engineering strain in correspondence to the ultimate strength, is similar among the *baseline*, *A0* and *A1* cases, the difference arises from the abrupt fracture propagation present in the *Ax* cases. In the *A2* case, the fracture occurred before the necking, resulting in lower ductility and ultimate strength.

The aging treatment significantly enhanced the strength of both the *baseline* and *A2* cases, with an increase of about 100% and 50% for the yield and ultimate strength, against a marked ductility reduction compared to the as-built material, Fig. 9 (b). The aging treatment did not alter the differences observed between the *baseline* and *A2* set: while the yield strength of the *A2* case is slightly greater than the *baseline* one, the elongation at fracture is lower by about 50%, as reported in Table 4. Due to the absence of necking, the ultimate strength resulted to be affected by ductility reduction.

As shown in Fig. 10, the fracture surface is characterized by a central region almost orthogonal to the specimen loading direction, while the outer ring presents surfaces angled at about 45°. The cup-cone shape is more evident in the *as-built* specimens, as typical for specimens with elevated ductility, while aged specimens showed a wider flat central region. The principal difference between the *baseline* and the *Ax* specimens arises from the presence of pores and lack of fusion

regions, marked by white arrows in Fig. 10. In particular for the *A1* and *A2* cases, Fig. 10 (c, d, f), the fracture occurred on a section that was weakened by a significant presence of a wider defect or an area rich of small lack of fusion zones. The presence of such defects could have played the principal role in determining the reduction of the elongation at fracture observed for the *Ax* sets.

Young's modulus, calculated as the angular coefficient of the tangent to the elastic region of the stress-strain curve (up to a maximum stress value of 1/5 of the yield strength), was found not to be significantly affected by the SLM parameters set in the as-built case. For the aged specimens, the *A2* set presented a value 15% greater than the *baseline*. It is worth noticing that the evaluation of Young's modulus from the tangent to the stress-strain curve is intrinsically affected by strong uncertainty, in particular when the specimen features an elevated surface roughness.
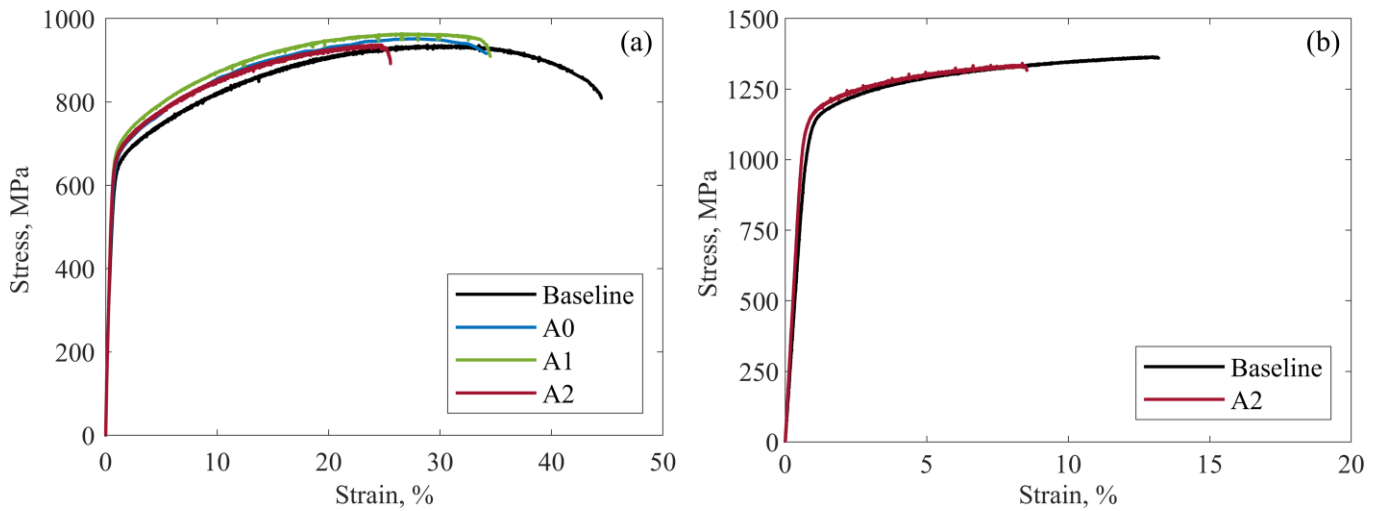

Fig. 9. Representative engineering tensile curves: as-built (a) and aged (b) conditions.

	As-built				*Aged*	
	Baseline	*A0*	*A1*	*A2*	*Baseline*	*A2*
S_y, MPa	500 ± 20	540 ± 20	615 ± 10	615 ± 10	1100 ± 10	1135 ± 5
S_u, MPa	920 ± 10	950 ± 10	960 ± 10	930 ± 15	1350 ± 15	1330 ± 10
%EL, %	43 ± 2	33 ± 2	34 ± 2	24 ± 5	15 ± 2	7 ± 2
UE, %	31 ± 2	28 ± 1	27 ± 2	22 ± 5	15 ± 2	7 ± 2
E, GPa	139 ± 7	142 ± 8	138 ± 7	135 ± 5	155 ± 5	180 ± 5

Table 4. Tensile properties in the as-built and aged material conditions.
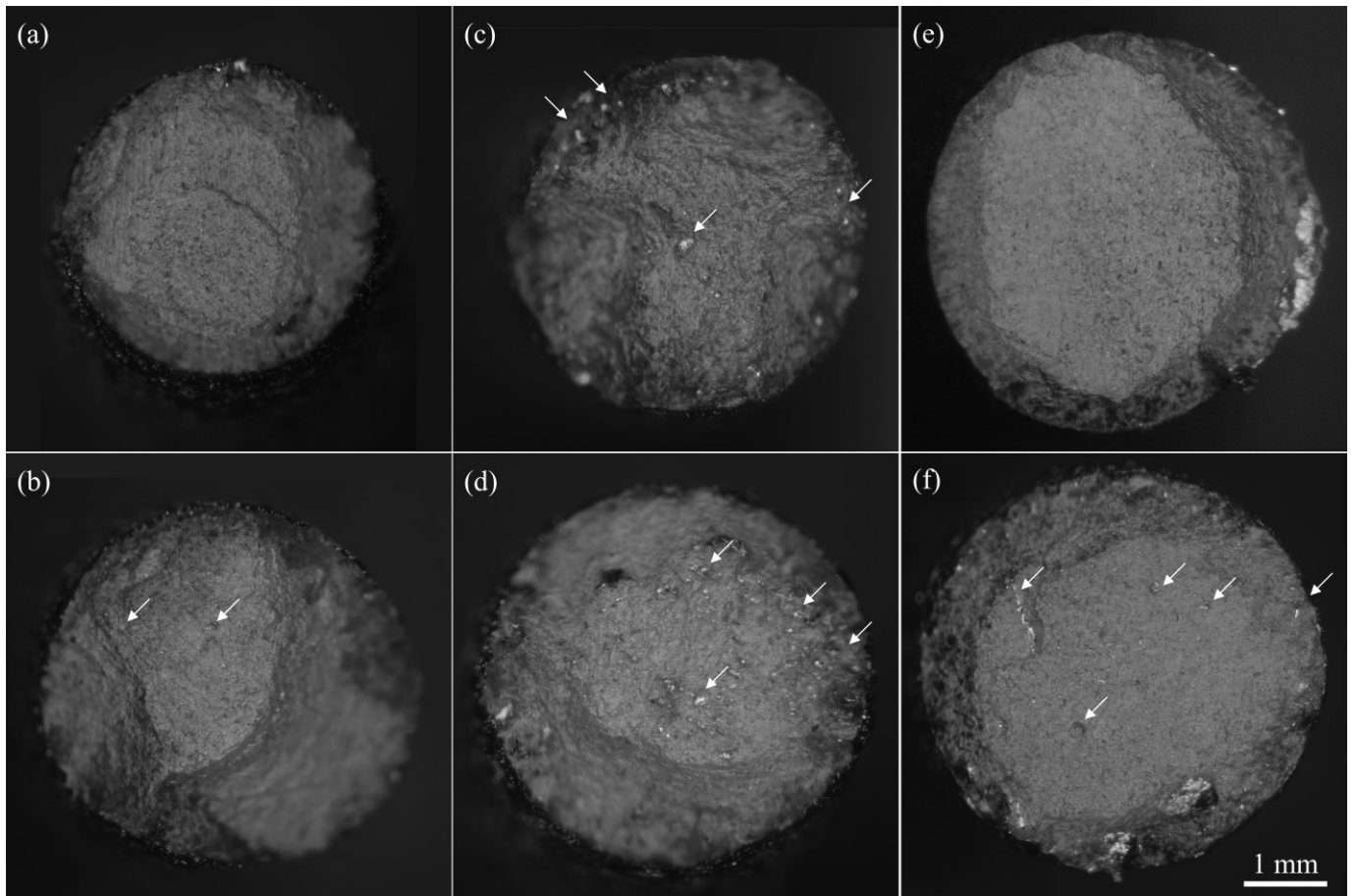
Fig. 10. Fracture surfaces of the specimens undergone tensile tests, observed via stereomicroscope. As-built condition (a-d): (a) baseline, (b) A0, (c) A1, and (d) A2 sets. Aged-condition (e-f): (e) baseline, and (f) A2 sets. White arrows point out the lack of fusion regions or significant pores.

The material hardness was investigated along two orthogonal diametral lines on the specimen transverse section, measuring the effective position of the indentation center after the test. The average value on the whole section and the outer region, defined as the ring that extends up to 1.2mm deep from the specimen surface, are listed in Table 5.

For the *baseline* condition, the hardness resulted to be almost uniform in the whole section, with average values of 289 ± 2 HV, in the as-built condition, and 457 ± 2 HV in the aged condition, in line with values reported in the literature, [16]. In the as-built condition, the *Ax* sets were found to negligibly affect the average section hardness, which presented values slightly greater than the *baseline* case, Table 5. A greater increase in the material hardness was observed in the outer region, with a wider difference for the *A2* case. It could arise from a higher temperature gradient experienced by the outer region of the *Ax* specimens, due to the increased scanning velocity and the usage of the same process parameters for both the hatching and contour region, differently from the *baseline* set. This effect turned out to vanish for the aged specimens, which presented a similar average hardness for the *baseline* and *A2* cases and a uniform hardness on the whole section, as reported in Table 5.

| | As-built | | | | Aged | |
	Baseline	*A0*	*A1*	*A2*	*Baseline*	*A2*
Average value	283 ± 2	289 ± 2	288 ± 2	286 ± 3	456 ± 2	457 ± 3
Outer region	283 ± 3	291 ± 2	291 ± 3	295 ± 3	457 ± 3	456 ± 3

Table 5. Vickers hardness values for sections extracted in the specimen transverse direction.

3.4. Fatigue results

The fatigue data for the tested process parameters sets, both in the as-built and aged material condition, are presented through S-N diagrams in Fig. 11 and Fig. 12, along with the fitting line and confidence bands corresponding to 50%, 2.5%, and 97.5% probability of failure, respectively. The fatigue strength, expressed in terms of stress range ($\Delta\sigma$) at 1 million cycles to failure, along with the inverse slope of the fitting line (m), the scatter parameter ($T_{\Delta\sigma}$), and the variance (σ) for the normal distribution of log(N) is listed in Table 6.

Notwithstanding the increased material porosity and surface roughness, the S-N curves were found to be only slightly affected by the tested sets of process parameters. In Fig. 11 (a-d) and Fig. 12 (a), the data belonging to the specimens tested in the as-built material condition are presented. The linearized S-N curves resulted to be almost parallel within the investigated cycles range: the inverse slope of the fitting line, m, is identical for the *baseline*, *A1*, and *A2* sets, about 3.55, while it turned out to be slightly lower for the *A0* case, 3.09, as listed in Table 6. Apart from the *A1* case, the *Ax* data present a lower scatter, with a $T_{\Delta\sigma}$ of 1.2 against 1.39 of the *baseline* set. The fatigue strength of the *Ax* sets turned out to be lower than the *baseline* case but still comparable, Fig. 12 (a). The *A2* set, despite the significant increase in the surface roughness and material porosity, presented a fatigue strength lower only by 5% than the *baseline* reference. The *A1* set, instead, presented a reduction of 12%.

The *baseline* and *A2* sets were also tested in the aged condition. Their fatigue data are presented by means of S-N curves in Fig. 11 (e-f) and Fig. 12 (b), while the numerical values are listed in Table 6. The fatigue strength of the *A2* set resulted to be lower by about 4% compared to the *baseline* case, with values of 313 MPa and 301 MPa. The aging treatment increased the fatigue strength by 30% for both the investigated sets. The greatest deviation between the two S-N curves occurs in the long-life region, since the *A2* case presented a steeper curve, with an inverse slope of 3.57 against 3.81 for the *baseline* set. Notwithstanding the increase in the surface roughness and material porosity of the *A2* set, the scatter of the data resulted to be identical, with a scatter index of 1.32. The S-N curves of the *baseline* and *A2* sets presented the same relative behavior in the aged and as-built conditions, in terms of fatigue strength ratio, curve slope and data scatter, notwithstanding the ductility reduction and the strength growth.

The crack propagation rate was indirectly investigated by monitoring the operating frequency of the resonant machine employed for the HCF test. For all the tested sets, both in the as-built and aged condition, the frequency remains almost constant until a sudden drop happens, in correspondence to the occurrence of a macroscopic crack propagation phase

before the final fracture, as shown in Fig. 13 for the *baseline* and *A2* cases. If we consider the detection of macroscopic nucleation in correspondence to a frequency drop of 0.05 Hz, the crack propagation took almost 5% of the fatigue life for all the investigated cases. The crack propagation behavior is similar for all the tested parameters, affecting the fatigue life detection in the same way.
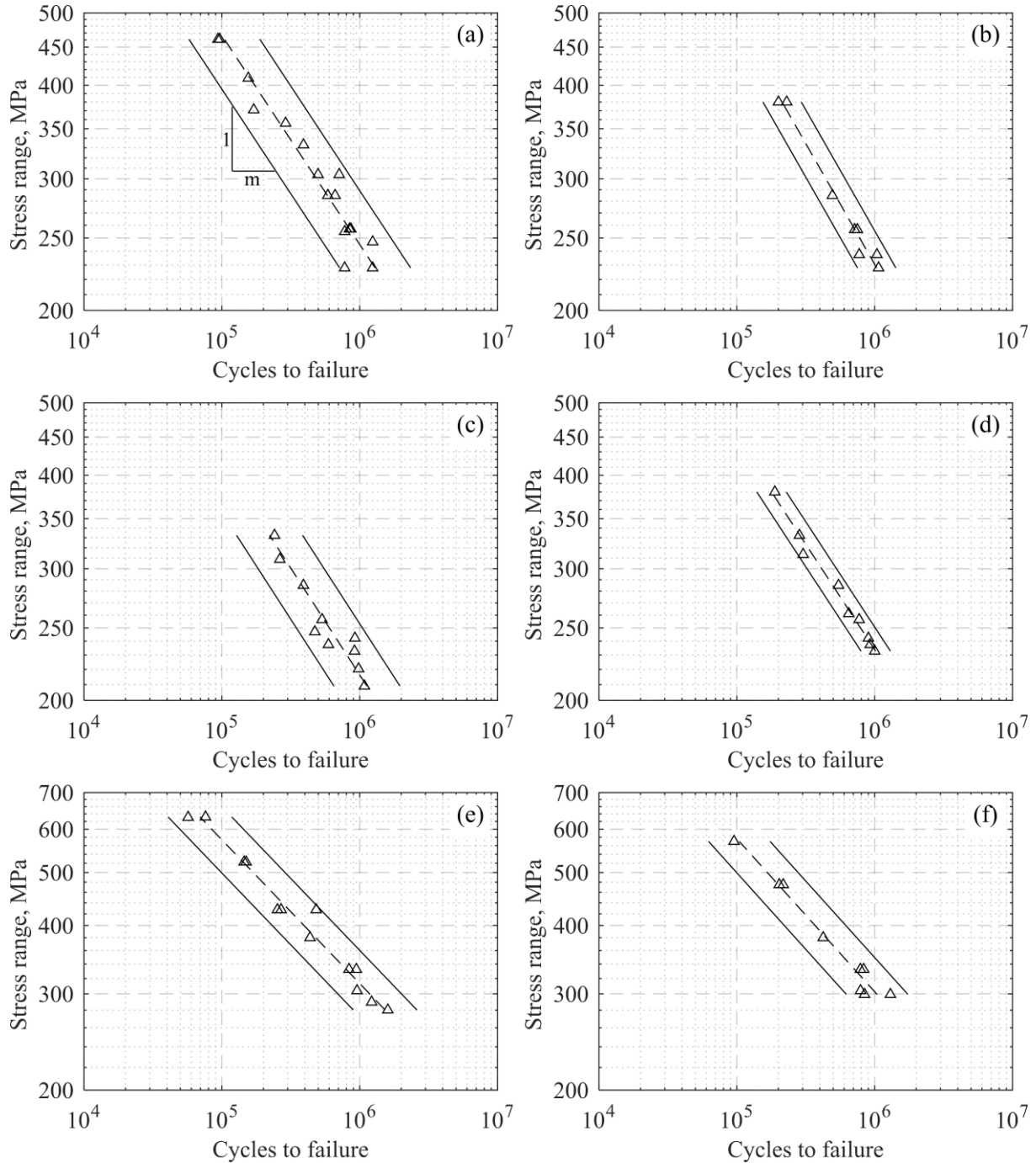

Fig. 11. S-N curves in the as-built condition for the *baseline* (a), *A0* (b), *A1* (c), and *A2* (d) process parameters set, and in the aged condition for the *baseline* (e), and *A2* (f) set. Scatter bands calculated at 97.5% and 2.5% probability of failure and a 0.9 confidence level.
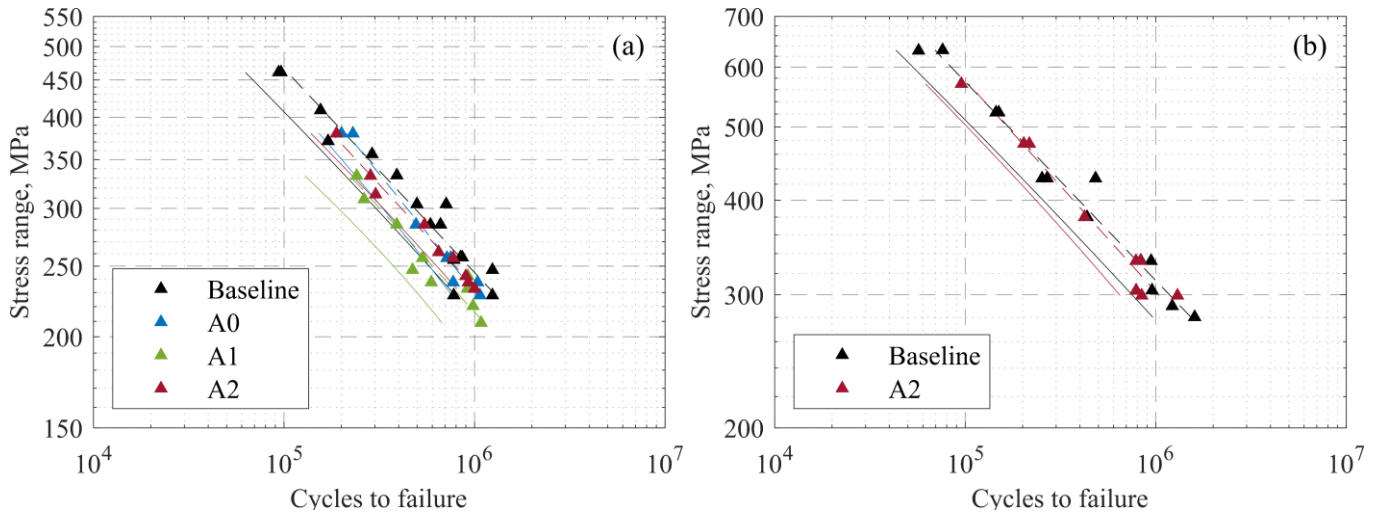
Fig. 12. S-N curves in the as-built (a) and aged condition (b) for all the tested sets. Lower prediction limit at 90% failure probability and 0.95 confidence level (continuous line) evaluated according to ISO 12107.

	As-built				Aged	
	Baseline	*A0*	*A1*	*A2*	*Baseline*	*A2*
m	3.57	3.09	3.50	3.55	3.81	3.57
R^2	0.94	0.98	0.90	0.99	0.97	0.97
σ	0.10	0.04	0.08	0.03	0.08	0.07
$T_{\Delta\sigma}$	1.39	1.23	1.37	1.15	1.32	1.33
$\Delta\sigma_{50\%}$ [MPa]	245	230	216	234	313	301
$\Delta\sigma_{97.5\%}$ [MPa]	208	208	185	218	272	262
$\Delta\sigma_{2.5\%}$ [MPa]	289	256	253	251	360	349

Table 6. Values for the S-N curve: slope (m), coefficient of determination (R^2), scatter index ($T_{\Delta\sigma}$), variance for the log(N) normal distribution (σ), stress range and confidence bands at 97.5% and 2.5% probability of failure, at $1\cdot10^6$ cycles.
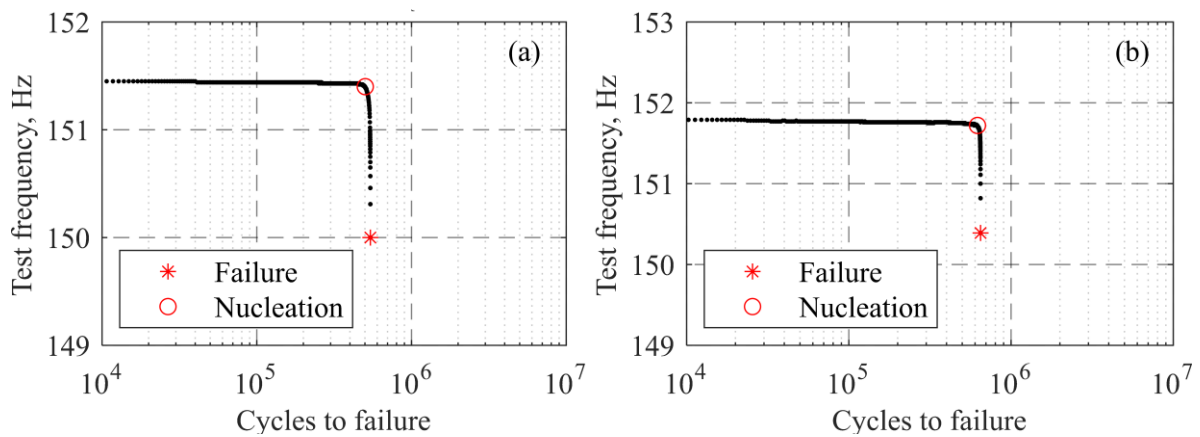

Fig. 13. Crack onset detection by monitoring the test frequency, *baseline,* (a) and *A2* (b) process parameters.

3.5. Mean stress effects on the fatigue strength

The fatigue strength sensitivity to the mean stress effect, in the as-built material condition, was investigated by testing a batch of *baseline* specimens for three load ratios, -1, 0.05, and 0.4.

The material resulted to be utterly insensitive to the mean stress, showing S-N curves that are almost indistinguishable in

the range between $2 \cdot 10^5$ and $1 \cdot 10^6$ cycles, Fig. 14 (a). The curve slope of the R 0.05 and R -1 curves is almost identical, while the R 0.4 showed a more horizontal curve. For the latter case, it was not investigated the higher stress range, due to the approaching yield strength value for the maximum stress.

As shown in Fig. 14 (b), the experimental behavior can not be rationalized in the framework of the Goodman or the Smith-Watson-Topper models, [43]. If we consider the more general model devised by Walker, [44]:

$$\sigma_{ar} = \sigma_{max}^{\gamma-1} \ \sigma_a^{\gamma} = \sigma_a \left(\frac{2}{1-R} \right)^{1-\gamma} \tag{10}$$

where σ_{ar}, σ_a, and σ_{max} are the equivalent fully reversed stress amplitude, the stress amplitude, and the maximum value over time, respectively, the material mean stress sensitivity is expressed in terms of the γ parameter, which assumes the asymptotic value of 1 in case of complete mean stress insensitivity. The γ parameter was numerically evaluated by fitting the fatigue life data at various mean stresses as a whole, [43], leading to a value of about 1.

The mean stress insensitivity points out the presence of the elevated residual stresses along the specimen build direction, parallel to the loading axis, that are well known to be intrinsic in the SLM process in the as-built condition, [35,45,46]. The effective stress ratio in proximity to the region of fatigue crack onset, namely the specimen surface, is thus different from the nominal one, as the local residual stresses have to be added to the stresses arising from the external loads. Even in the presence of elastic nominal strains, a local yielding can occur.

Since the residual stresses are almost canceled by the adopted aging treatment, the Smith – Watson - Topper model was adopted in the case of the aged specimens, as reported in the literature, [16]. Therefore, the mean stress sensitivity parameter, γ, assumes a value of 0.5.
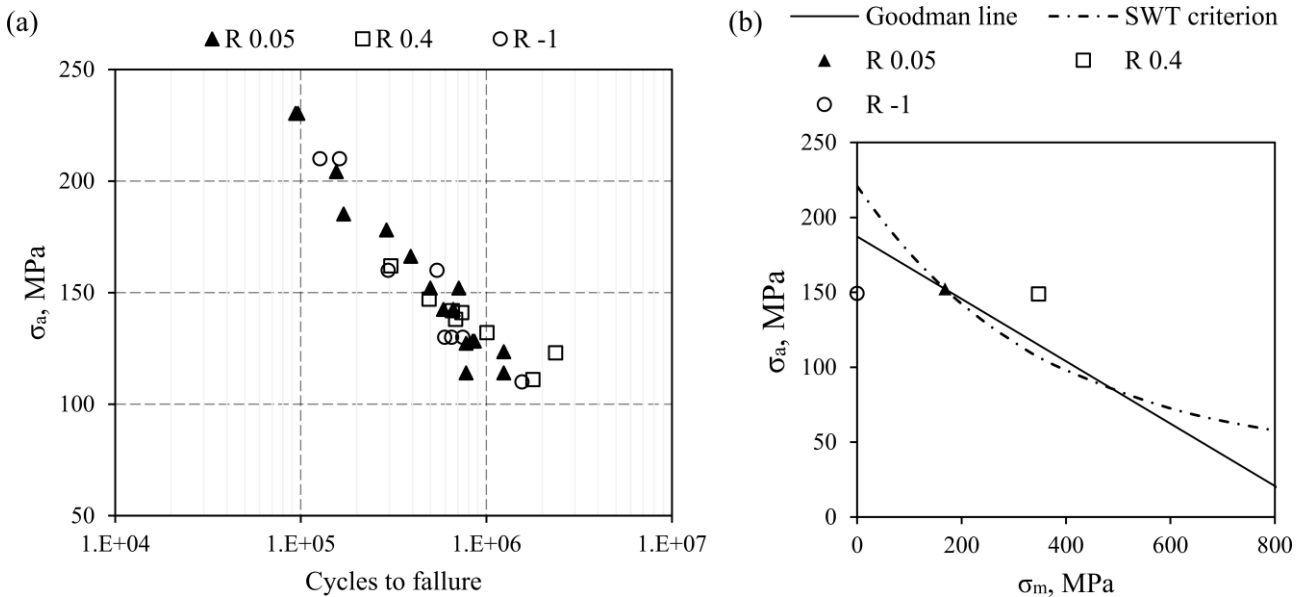

Fig. 14. S-N curves obtained with different load ratios for the *baseline* set in the as-built condition (a); Haigh diagram built in correspondence of a fatigue life of $8 \cdot 10^5$ cycles (b).

3.6. Fractographic analysis

The fractographic examination carried out by stereomicroscope and SEM showed that, in the case of the as-built condition, the fatigue crack occurred on the specimen surface, in correspondence with local irregularities of the surface roughness, for all the tested specimens, as shown in Fig. 15. The fracture surface presented a similar aspect for all the tested sets, both in the crack nucleation, first propagation, and fracture growth regions. The fracture arose from a single nucleation region, pointed out by a white arrow, and propagated along a plane orthogonal to the loading direction until the final rupture occurred. As shown in Fig. 15 (k), in some cases of the *Ax* sets, a Secondary Crack (SC) occurred on a parallel plane and propagated until it joined the principal propagation, with the formation of ratchet marks. The extension of the onset, propagation and final fracture regions can be observed through the change of the surface brightness in the stereomicroscope observations, reported in the left column of Fig. 15, from a brighter surface near the onset to a darker surface in correspondence to the final shear lip.

The right column of Fig. 15 reports the detail of the region surrounding the crack onset. For all the cases, it can be observed that the fracture propagates from the apex of a deep surface valley, in correspondence to an additional waviness along the hoop direction that introduced a further stress concentration, in particular for *baseline* and *A0* sets, Fig. 15 (c) and (f).

In the case of the *A1* set, for several specimens the fracture arose from macroscopic defects present on the surface, consisting of a local area of lack of fusion on the external surface probably due to instabilities in the meltpool and to an uneven powder spread caused by the wear of the recoater wiper produced by raised borders, Fig. 15 (g-i). However, also these defects appeared as notches open to the external surface, namely as deeper valleys of the surface roughness profile. In the case of *A2* specimens, the fatigue crack propagated from irregular regions of the specimen profile, but no marked lack of fusion defects were observed, Fig. 15 (l). The irregularity of the surface profile led to a visible difference in the region of the first crack propagation. While a pattern of propagation ridges is clearly observable in the *baseline* case, Fig. 15 (c), a more jagged surface appears in the *Ax* cases. It could be due to the presence of a wider region subjected to elevated stresses, which arise from the more severe stress concentration consequent to the poor surface finish. Due to the elevated ductility of the material, transgranular cleavage facets can be observed only on the utmost initial portion of the crack onset. In proximity to the fracture onset, no significant pores were observed.
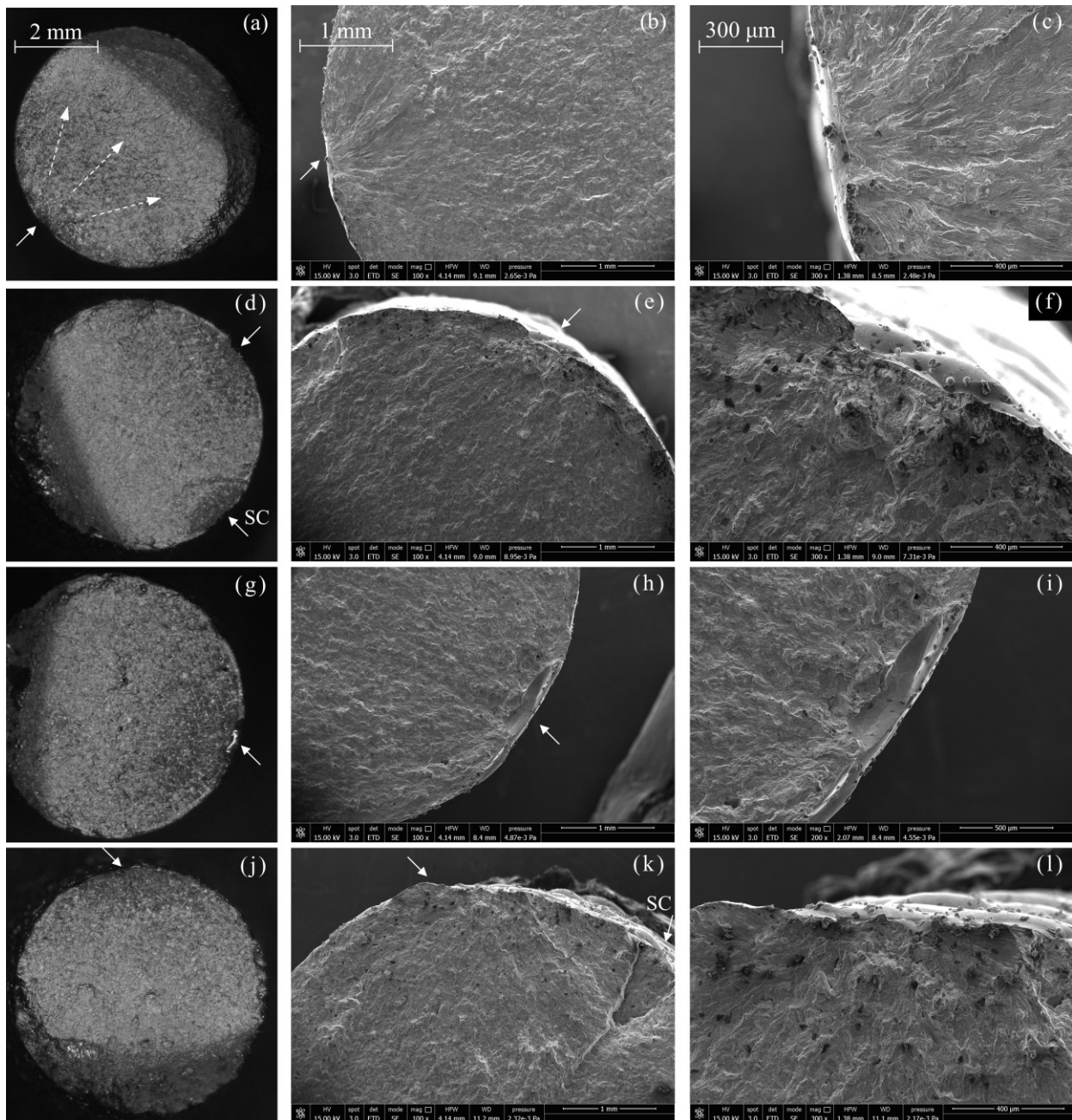
Fig. 15. Stereomicroscope and SEM images of the fracture onset and fatigue crack propagation regions, as-built condition: (a-c) *baseline,* (d-f) *A0,* (g-i) *A1,* (j-l) *A2* sets. Cycles to failure $N_f = 5.8 \cdot 10^5$, $N_f = 7.7 \cdot 10^5$, $N_f = 6.0 \cdot 10^5$, and $N_f = 9.3 \cdot 10^5$.

The fracture surfaces of the aged specimens presented the same features as the as-built ones. For all the tested specimens, the fatigue crack nucleated from surface defects, and the fracture surface resulted to be orthogonal to the loading direction, as typical of tensile mode propagation. In the case of the *baseline* condition, Fig. 16 (a) and (d), the fracture onset was found at the apex of a surface roughness valley, in correspondence to an undulation along the specimens' hoop direction. A transgranular fragile region and cleavage facets can be observed near the specimen surface, Fig. 16 (d). Compared to the observation of the as-built specimens, the cleavage region was found to be wider, in light of the material hardening introduced by the aging treatment. In the case of the *A2* set, the surface roughness discontinuities are deeper and more irregular, but the fracture growth is similar to the *baseline* set for most of the specimens, Fig. 16 (b) and (e). However,

for some specimens of the *A2* set, the crack arose from lack of fusion defects present in proximity to the surface roughness valleys, at least partially open to the surface, Fig. 16 (c) and (f). The surface roughness further affected the fatigue crack growth by seldom causing the occurrence of secondary cracks that speed up the fracture propagation or caused a shift of the crack propagation between parallel planes.

The fatigue crack growth rate, investigated by the striations orthogonal to the crack propagation, was not substantially affected by the *A2* set, keeping the features reported in the literature for the aged Inconel 718, [34,41].

Significant lack of fusion defects and pores were detected in the inner region of the *A2* specimens, far from the crack nucleation region. In some cases, the presence of a pattern of lack of fusion defects caused an abrupt transition from the crack growth to the final fracture phase. However, as the crack propagation took a negligible portion of the fatigue life, this effect did not appreciably affect the fatigue strength.
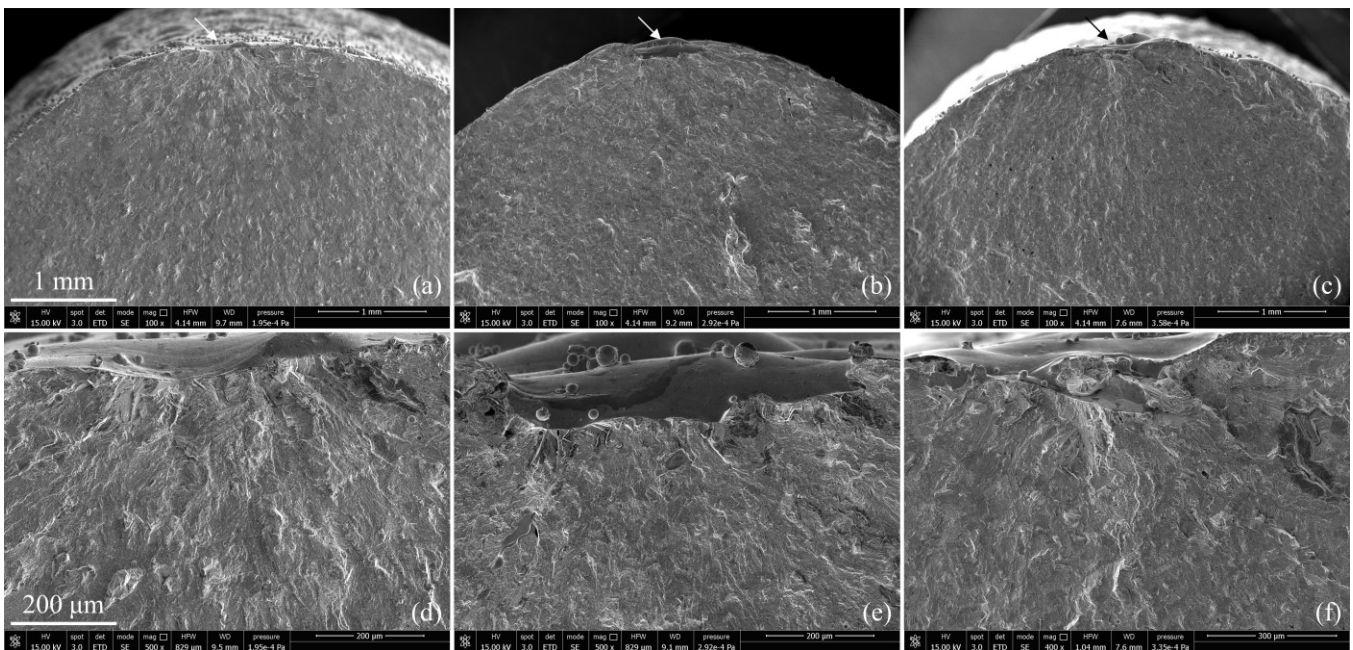

Fig. 16. SEM images of the fracture onset region for the aged material: (a and d) *baseline,* (b, c, e, and f) *A2* process parameters set. Fracture onset and fatigue crack propagation regions represented in images from (a) to (c). Details of the fracture onset area reported in images from (d) to (f). Cycles to failure $N_f = 1.2 \cdot 10^6$, $N_f = 7.9 \cdot 10^5$, and $N_f = 8.3 \cdot 10^5$.

The crack propagation region was also investigated through metallographic sections extracted in the specimen's longitudinal direction, orthogonal to the fracture plane, and parallel to the crack propagation direction. It is not significantly affected by the investigated process parameters, Fig. 17 (a and b). The crack propagates orthogonally to the loading direction (mode I) and proceeds through adjacent meltpools in a transgranular propagation, without any decohesion phenomena along the meltpool boundaries for all the tested sets. This behavior is in line with the literature data for fatigue crack propagation in full dense SLMed Inconel 718, [34,41].
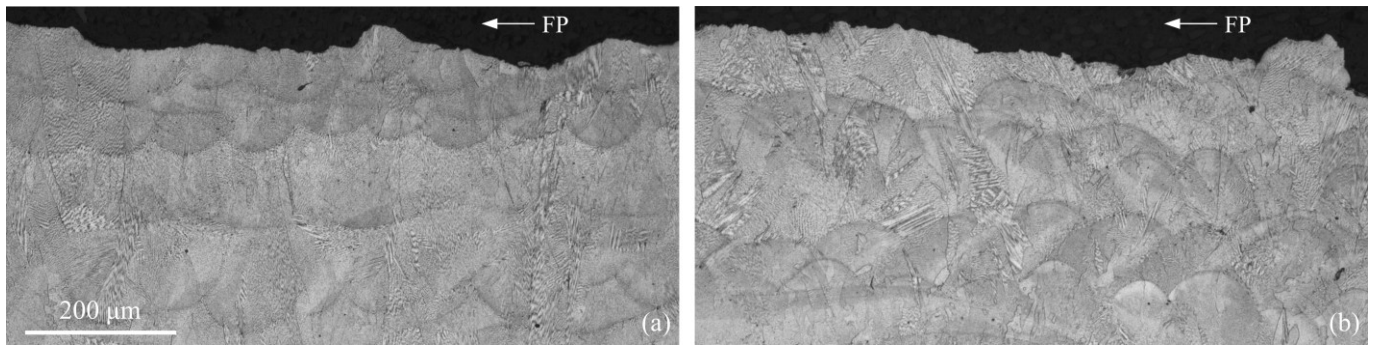
Fig. 17. Detail of the fatigue crack propagation for *baseline* (a) and *A2* (b) specimens, As-built condition, cycles to failure $N_f = 8 \cdot 10^5$, $N_f = 9 \cdot 10^5$, respectively. Fracture propagation direction identified by marker "FP". Etchant: Kalling's II.

Metallographic inspections, carried out after the fatigue testing, revealed a wide presence of non-propagating cracks, which were not observed in virgin specimens, hinting that material toughness and plasticity, i.e. plasticity-induced crack closure phenomena, [47], played a significant role in the fatigue behavior.

As shown in Fig. 18, non-propagating cracks originating from surface roughness irregularities were observed in all the tested sets. However, the cracks were markedly more frequent in the *Ax* cases. While in the *baseline* set, only a few cracks arising from isolated roughness irregularities were observed, Fig. 18(a), in the *Ax* case frequent non-propagating cracks arose from the bottom of the steeper or deeper surface roughness valleys, Fig. 18(b-f). The steeper valleys of the surface roughness acted thus as sharp notches, from whose root cracks originated. The fatigue fracture site was thus only the worst among a series of potential crack sites, supporting the choice of a specimen with a wide uniform test section.

The length of the cracks ranged from 20 μm to 110 μm, but in presence of concurrent sub-superficial porosity, their growth was enhanced due to the local stress concentration, reaching about 300 μm, as shown in Fig. 18 (f). A clear crack-stopping factor does not appear, suggesting that the fatigue limit is controlled by the average strength properties of the microstructure, [17].
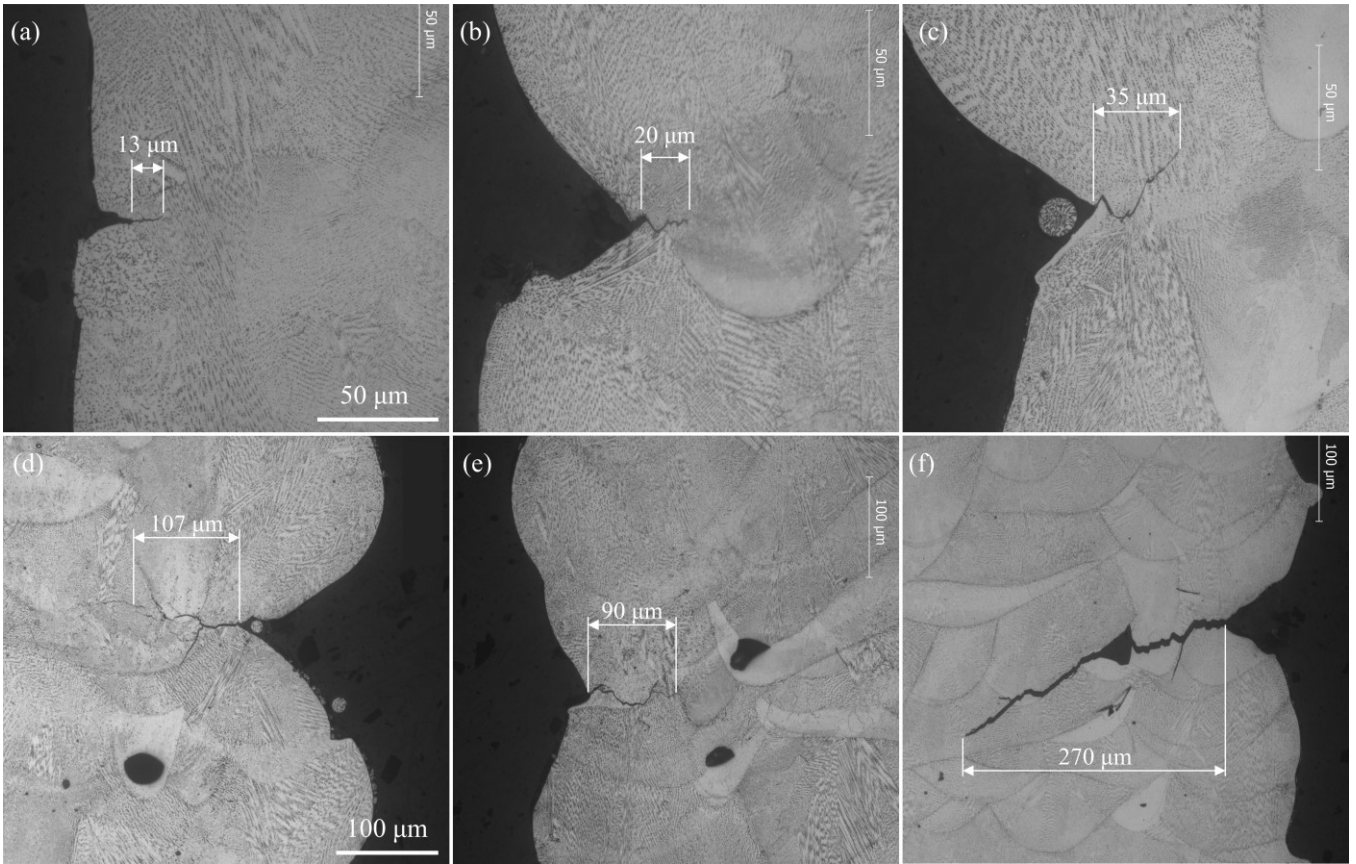
Fig. 18. Non-propagating cracks originating from the surface roughness valleys: short cracks for the *baseline* (a) and *A2* (b-c) specimens; longer cracks for the *A2* (d-e) and *A1*(f) sets. As-built condition, cycles to failure between $5 \cdot 10^5$ and $1 \cdot 10^6$. Etchant: Kalling's II

3.7. Near-surface stress field

The FE model describing the effective specimen profile showed the local stress concentration effect arising from the surface roughness valleys, with the stress peak occurring at the valley root, Fig. 19. In the *A2* case, the theoretical stress concentration factor (k_t), defined as the ratio of the maximum longitudinal stress with the nominal value, was found to be almost double the *baseline* one, as listed in Table 7. It is also worth noticing that even in the case of the *baseline* case, the effective stress is significantly greater than the value calculated for the nominal smooth specimen.

Fractographic investigations pointed out that surface roughness played a significant role in determining the fatigue strength of the specimen. However, the fatigue strength reduction factor is markedly lower than the increase in the relative k_{t_rel} value, defined by dividing the actual k_t with the *baseline* reference, or in the surface roughness descriptors. The localized and severe stress concentration caused by steep roughness valleys, which feature a root radius mostly comprised between 1 and 10 µm, suggests that the roughness problem has to be considered as a crack problem, rather than a notch one. Furthermore, an interference effect between consecutive valleys appears from the FE-predicted stress field, suggesting that the fatigue stress concentration is a property of the whole profile pattern.
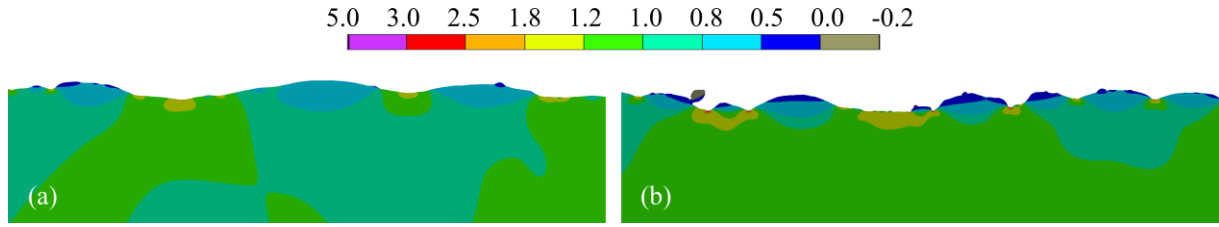
Fig. 19. Longitudinal stress predicted by the FE model describing the effective surface roughness profile, normalized with respect to the nominal stress occurring in the specimen gauge length: (a) *baseline* and (b) *A2* process parameters set.

	Baseline	*A2*
Rz, μm	42 ± 9	95 ± 20
k_t	2.7 ± 0.4	4.9 ± 1.8
k_{t_rel}	-	1.8 ± 0.4

Table 7. Surface roughness stress concentration effects compared with the *Rz* parameter.

3.8. Fatigue strength prediction

In light of the presence of several non-propagating cracks emanating from the apex of the surface roughness valleys, Fig. 18, the approach devised by Murakami, [17,24], which suggests that the fatigue limit of specimens with a surface roughness pattern is governed by the threshold condition for non-propagation of a crack emanating from the roughness valleys root, appears to be promising for the present case. Under the assumption that a periodic roughness valley is equivalent to periodic cracks, the fatigue strength is governed both by the valleys' depth and pitch due to the interference between notches, which can be condensed in the Murakami $\sqrt{area_R}$ parameter, [17,24]:

$$\sqrt{area_R} = \begin{cases} p\left(2.97\ \frac{a}{p} - 3.51\left(\frac{a}{p}\right)^2 - 9.74\left(\frac{a}{p}\right)^3\right) & for\ \ \frac{a}{p} \leq 0.195 \\ 0.38\,p & for\ \ 0.195 < \frac{a}{p} < 3 \end{cases} \tag{11}$$

where *a* is the valley's depth, and *p* is the pitch distance between two consecutive roughness valleys. The initial value of the $\sqrt{area_R}$ value of the equivalent crack is the crucial geometrical parameter that controls the fatigue limit.

As the surface roughness profile is highly irregular, the definition of *a* and *p* is not straightforward. The former was defined as the maximum among the *Rz* values, namely the maximum height of the profile within a sampling length, in agreement with [24]. A criterion for the pitch evaluation was defined on the basis of the stress field predicted by the FE model, considering both the peak values and size of the highly stressed areas to identify the critical regions, as shown in Fig. 20. In the case of the *Ax* sets, the roughness profile features a superposition of steep valleys and shallow irregularities, which do not cause a significant stress concentration. Their interaction plays a considerable effect in determining the stress field near the specimen surface, as the reduction of the valleys' pitch can contribute to shielding the stress concentration effects produced by the steeper ones, [18]. As illustrated in Fig. 20 (c) and (d), longitudinal sections, extracted from fatigued specimens, confirmed that non-propagating cracks arose from sharp and far valleys.
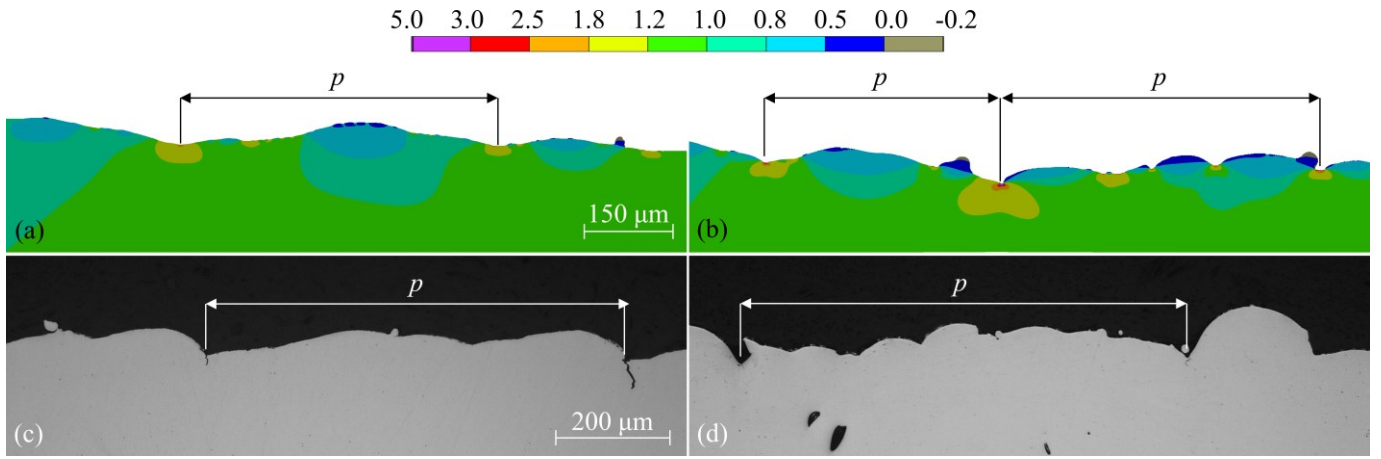
Fig. 20. Definition of the roughness valleys pitch employed in the Murakami model based on the stress field predicted by the FE model. Longitudinal stress field predicted for a specimen representative of the typical condition produced by *baseline (a)* and *A2* (b) sets. Steep valleys and non-propagating cracks observed for the *baseline (c)* and *A2* (d) sets.

Assuming that the pitch values are almost normally distributed, as shown in Fig. 8, the $\sqrt{area_R}$ parameter was calculated considering the longest possible pitch, with a probability of 99%, namely

$$p = \mu_p + 3\,\sigma_p \qquad\qquad (12)$$

where μ_p and σ_p are the mean and the standard deviation of the pitch distribution.

The estimated values of the $\sqrt{area_R}$, listed in Table 8, resulted to be comprised in the range $160 \div 300$ μm, lower than the long cracks threshold (1000 μm), [17,48]. The profile valleys' depth and pitch ratio (a/p) falls between 0.06 and 0.2, with extreme values occurring for the *baseline* and *A1* sets, respectively. In Fig. 21, equation (11) is employed to plot the $\sqrt{area_R}$ parameter as a function of the valleys' depth and pitch. The values calculated from the analyzed profiles are reported as well, to investigate their sensitivity to pitch or depth variations. The *A1* and *A2* sets fall within the region that features a limited sensitivity to the valley's depth, while they are sensitive to pitch variations. The opposite holds for the *baseline* case. It is worth noting that when the ratio a/p overcomes 0.195, the variations of the $\sqrt{area_R}$ parameter depends only on the pitch, as shown by the horizontal lines and the coincident curves in Fig. 21 (a) and (b), respectively.
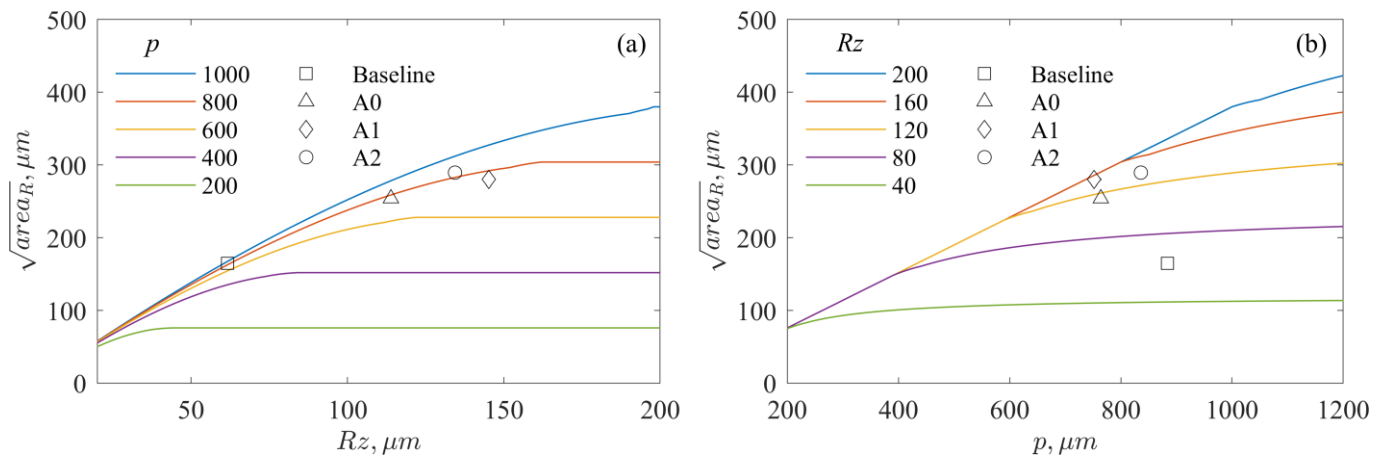

Fig. 21. Murakami $\sqrt{area_R}$ parameter, as a continuous function of the valleys' height (a) and pitch (b).

The theoretical fatigue strength, σ_w, can be thus predicted on the basis of the knowledge of the average $\sqrt{area_R}$ parameter,

the Vickers hardness, the applied load ratio R, and the material mean stress sensitivity:

$$\sigma_w = \frac{1.43\,(H_V + 120)}{\sqrt{area_R}^{1/6}} \left(\frac{1-R}{2}\right)^{\gamma-1} \qquad (13)$$

where it was considered the hardness value of the outer ring of the specimen. The model was found to overestimate the fatigue strength both for the as-built and aged material condition for all the tested sets, but it effectively predicted the fatigue strength reduction experimentally observed for the *Ax* sets, with a maximum error of 5%.

Applications of the Murakami approach to additive manufactured materials suggested that the fatigue strength of the defect-free material, defined only on the material's hardness, is far from the experimental data. It arises from the intrinsic presence of macroscopic and microstructural defects, [17,21]. Indeed, the Murakami $\sqrt{area}$ model resulted to be effective in predicting the occurrence of failure when the killer defect area was considered per each specimen, [15,16,21,48–51]. The $\sqrt{area_R}$ parameter considers only a surface roughness profile in the specimen longitudinal direction, while the as-built surface produced by SLM presents also a marked surface roughness along the specimen hoop direction, as shown in Fig. 16 and Fig. 17. As the material produced by SLM is not defect-free even if the surface roughness is null, we can model the effects peculiar of the SLM process by modifying the hardness offset value, which can be defined by fitting the predicted and experimental fatigue strength values for the *baseline* case in the material as-built condition. The correlation between the $\sqrt{area}$ parameter and the threshold stress intensity factor range (ΔK_{th}) is preserved. It yields to:

$$\sigma_w = \frac{1.43\,(H_V - 82)}{\sqrt{area_R}^{1/6}} \left(\frac{1-R}{2}\right)^{\gamma-1} \qquad (14)$$

As shown in Fig. 22 and Table 8, the model effectively predicts the fatigue strength for all the tested sets, both for the as-built and aged material. The ratio between the predicted and the experimental fatigue strength (σ_w/σ_e) falls between 0.96 and 1.08, as reported in the last column of Table 8. It is worth remarking that the fatigue strength of the *baseline* set for the aged material condition, which was not used in the fitting procedure, was successfully predicted.

In the case of the as-built *A2* specimens, against an increase of 120% in the surface profile height, the model predicted the same fatigue strength reduction experimentally observed (-5%). For the aged material, the model resulted to be slightly conservative, leading to a value lower than the experimental one by 5%.

The highest deviation between the predicted and the experimental values was observed for the *A1* case, which often presented the crack onset in proximity to surface defects that are more severe than the ones considered by the 2D surface roughness model hereby assumed, as shown in Fig. 16 (i). Furthermore, this set presented the highest pore area, Table 2. Even if no cracks were detected originating from an inner pore, the stress concentration due to subsurface pores could have enhanced the effects of the surface roughness. In the as-built case, the slight increase in the material hardness observed for the *Ax* specimens played a marginal role in the model prediction, while this effect vanishes in the aged ones.
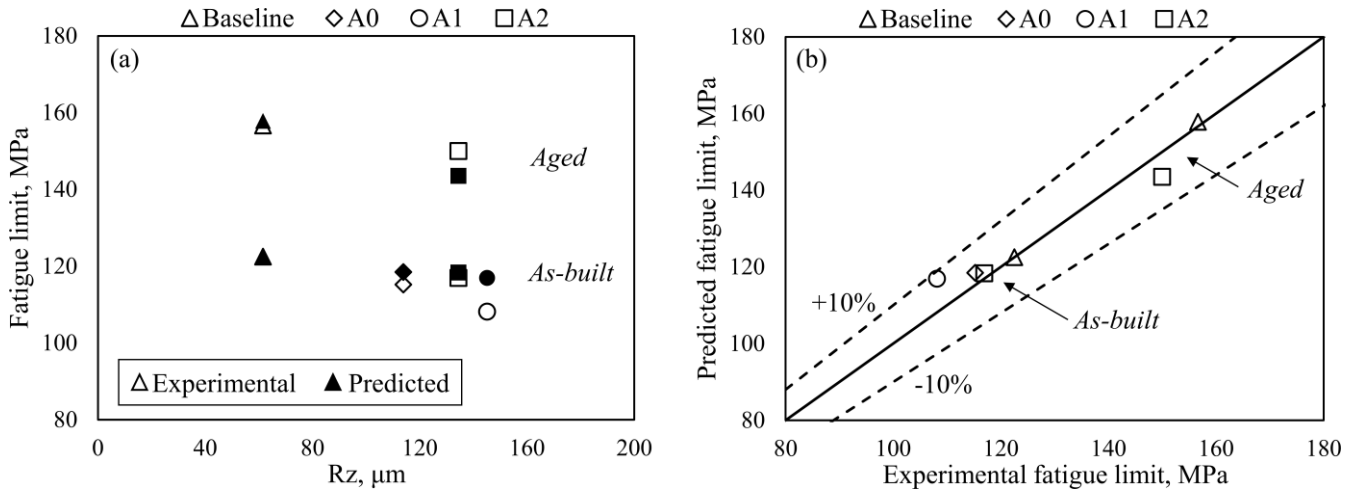
Fig. 22. Application of the Murakami $\sqrt{area_R}$ model in the formulation of eq. (14). Effect of the surface roughness height, *Rz,* on the predicted and experimental fatigue limit for as-built and aged material conditions (a); direct comparison between predicted fatigue limits and experimental results (b).

	Set	HV	Rz		Pitch	$\sqrt{area_R}$		$\sigma_{wR\,0.05}$		σ_e		σ_w/σ_a
			μm	Δ	μm	μm	Δ	MPa	Δ	MPa	Δ	
	Baseline	283	62		884	165		123		123		**1.00**
As-built	*A0*	291	114	85%	764	254	54%	118	-3%	115	-6%	**1.03**
	A1	291	145	136%	752	280	70%	117	-5%	108	-12%	**1.08**
	A2	295	134	118%	836	290	76%	118	-3%	117	-5%	**1.01**
Aged	*Baseline*	457	62		884	165		158		157		**1.01**
	A2	456	134	118%	836	290	76%	143	-9%	150	-4%	**0.96**

Table 8. Surface roughness effects on the fatigue strength analyzed through the Murakami approach, eq. (14). Experimental fatigue strength, σ_e, and the predicted one, σ_w, are expressed in terms of stress amplitudes.

4. Conclusions

Two sets of SLM process parameters aimed at significantly enhancing the productivity rate were devised on the basis of an analytical model of the temperature field nearby the meltpool region for the alloy Inconel 718. Their static mechanical properties and HCF behavior were investigated and compared with the standard and the fastest process parameters present in the recent literature. The main findings can be summarized as follows:

1. The proposed sets produced a full-dense material, though they increased the surface roughness and the area of the inner pores. The tensile properties are affected only in terms of elongation at fracture, while the material hardness was slightly enhanced, both for the as-built and aged conditions.

2. Both in the as-built and aged condition, the most promising set, *A2*, presented only a 5% fatigue strength reduction compared to the standard case, against a 50% enhancement in the process productivity and a 120% growth in the surface roughness height.

3. Fractographic analyses showed that the fatigue cracks nucleated from the specimen surface, in proximity to surface

roughness valleys root. Non-propagating cracks were sometimes detected at the apex of the roughness valleys.

4. The approach devised by Murakami for the assessment of the surface roughness effects on the fatigue limit effectively predicted the fatigue strength for all the tested sets of SLM process parameters, after tuning on the reference case. Further investigations will be necessary to explore the generality of the proposed approach for different materials and surface conditions.

Specific process parameters could be developed for the contour scan paths, minimizing the surface roughness, against a negligible reduction in the process productivity rate.

References

[1] Liu SY, Li HQ, Qin CX, Zong R, Fang XY. The effect of energy density on texture and mechanical anisotropy in selective laser melted Inconel 718. Materials and Design 2020;191. https://doi.org/10.1016/j.matdes.2020.108642.

[2] Balbaa M, Mekhiel S, Elbestawi M, McIsaac J. On selective laser melting of Inconel 718: Densification, surface roughness, and residual stresses. Materials and Design 2020;193:108818. https://doi.org/10.1016/j.matdes.2020.108818.

[3] Tucho WM, Cuvillier P, Sjolyst-Kverneland A, Hansen V. Microstructure and hardness studies of Inconel 718 manufactured by selective laser melting before and after solution heat treatment. Materials Science and Engineering A 2017;689:220–32. https://doi.org/10.1016/j.msea.2017.02.062.

[4] Calandri M, Yin S, Aldwell B, Calignano F, Lupoi R, Ugues D. Texture and microstructural features at different length scales in Inconel 718 produced by selective laser melting. Materials 2019;12. https://doi.org/10.3390/ma12081293.

[5] Guo C, Li S, Shi S, Li X, Hu X, Zhu Q, et al. Effect of processing parameters on surface roughness, porosity and cracking of as-built IN738LC parts fabricated by laser powder bed fusion. Journal of Materials Processing Technology 2020;285:116788. https://doi.org/10.1016/j.jmatprotec.2020.116788.

[6] Ravichander BB, Amerinatanzi A, Moghaddam NS. Study on the effect of powder-bed fusion process parameters on the quality of as-built in718 parts using response surface methodology. Metals 2020;10:1–18. https://doi.org/10.3390/met10091180.

[7] Wan HY, Zhou ZJ, Li CP, Chen GF, Zhang GP. Effect of scanning strategy on grain structure and crystallographic texture of Inconel 718 processed by selective laser melting. Journal of Materials Science and Technology 2018;34:1799–804. https://doi.org/10.1016/j.jmst.2018.02.002.

[8] Yakout M, Elbestawi MA, Veldhuis SC. A study of the relationship between thermal expansion and residual stresses in selective laser melting of Ti-6Al-4V. Journal of Manufacturing Processes 2020;52:181–92. https://doi.org/10.1016/j.jmapro.2020.01.039.

[9] Watring DS, Carter KC, Crouse D, Raeymaekers B, Spear AD. Mechanisms driving high-cycle fatigue life of as-built Inconel 718 processed by laser powder bed fusion. Materials Science and Engineering A 2019;761:137993. https://doi.org/10.1016/j.msea.2019.06.003.

[10] Ferro P, Meneghello R, Savio G, Berto F. A modified volumetric energy density–based approach for porosity assessment in additive manufacturing process design. International Journal of Advanced Manufacturing Technology 2020;110:1911–21. https://doi.org/10.1007/s00170-020-05949-9.

[11] Moda M, Chiocca A, Macoretta G, Monelli BD, Bertini L. Technological implications of the Rosenthal solution for

a moving point heat source in steady state on a semi-infinite solid. Materials & Design 2022;223:110991. https://doi.org/10.1016/j.matdes.2022.110991.

[12] Moda M. Modeling of Powder Bed Fusion Additive Manufacturing. University of Pisa, 2021. https://doi.org/10.13131/etd/03092021-124517.

[13] Scime L, Beuth J. Melt pool geometry and morphology variability for the Inconel 718 alloy in a laser powder bed fusion additive manufacturing process. Additive Manufacturing 2019;29:100830. https://doi.org/10.1016/j.addma.2019.100830.

[14] Ferro P, Fabrizi A, Berto F, Savio G, Meneghello R, Rosso S. Defects as a root cause of fatigue weakening of additively manufactured AlSi10Mg components. Theoretical and Applied Fracture Mechanics 2020;108:102611. https://doi.org/10.1016/j.tafmec.2020.102611.

[15] Benedetti M, Fontanari V, Bandini M, Zanini F, Carmignato S. Low- and high-cycle fatigue resistance of Ti-6Al-4V ELI additively manufactured via selective laser melting: Mean stress and defect sensitivity. International Journal of Fatigue 2018;107:96–109. https://doi.org/10.1016/j.ijfatigue.2017.10.021.

[16] Solberg K, Wan D, Berto F. Fatigue assessment of as-built and heat-treated Inconel 718 specimens produced by additive manufacturing including notch effects. Fatigue and Fracture of Engineering Materials and Structures 2020;43:2326–36. https://doi.org/10.1111/ffe.13300.

[17] Murakami Y. Metal Fatigue. Elsevier; 2019. https://doi.org/10.1016/C2016-0-05272-5.

[18] Murakami Y, Endo M. Effects of defects, inclusions and inhomogeneities on fatigue strength. International Journal of Fatigue 1994;16:163–82. https://doi.org/10.1016/0142-1123(94)90001-9.

[19] Murakami Y. Material defects as the basis of fatigue design. International Journal of Fatigue 2012;41:2–10. https://doi.org/10.1016/j.ijfatigue.2011.12.001.

[20] Beretta S, Romano S. A comparison of fatigue strength sensitivity to defects for materials manufactured by AM or traditional processes. International Journal of Fatigue 2017;94:178–91. https://doi.org/10.1016/j.ijfatigue.2016.06.020.

[21] Yamashita Y, Murakami T, Mihara R, Okada M, Murakami Y. Defect analysis and fatigue design basis for Ni-based superalloy 718 manufactured by selective laser melting. International Journal of Fatigue 2018;117:485–95. https://doi.org/10.1016/j.ijfatigue.2018.08.002.

[22] Masuo H, Tanaka Y, Morokoshi S, Yagura H, Uchida T, Yamamoto Y, et al. Influence of defects, surface roughness and HIP on the fatigue strength of Ti-6Al-4V manufactured by additive manufacturing. International Journal of Fatigue 2018;117:163–79. https://doi.org/10.1016/j.ijfatigue.2018.07.020.

[23] Xu Z, Liu A, Wang X, Liu B, Guo M. Fatigue limit prediction model and fatigue crack growth mechanism for selective laser melting Ti6Al4V samples with inherent defects. International Journal of Fatigue 2021;143:106008. https://doi.org/10.1016/j.ijfatigue.2020.106008.

[24] Murakami Y, TsutsumiI K, Fujishima M. Quantitative Evaluation of Effect of Surface Roughness on Fatigue Strength. Transactions of the Japan Society of Mechanical Engineers Series A 1996;62:1124–31. https://doi.org/10.1299/kikaia.62.1124.

[25] Rosenthal D. The Theory of Moving Sources of Heat and Its Application to Metal Treatments. Transactions ASME 1946;43:849–66.

[26] Zhang H, Gu D, Ma C, Guo M, Wang R, Yang J, et al. Microstructure and tribological property of selective laser melted Ni-based composites using different scanning strategies. Vacuum 2020;177:109439. https://doi.org/10.1016/j.vacuum.2020.109439.

[27] Wang Y, Lu Y, Mendez PF. Scaling expressions of characteristic values for a moving point heat source in steady state on a semi-infinite solid. International Journal of Heat and Mass Transfer 2019;135:1118–29. https://doi.org/10.1016/j.ijheatmasstransfer.2019.02.042.

[28] Mendez PF, Lu Y, Wang Y. Scaling analysis of a moving point heat source in steady-state on a semi-infinite solid. Journal of Heat Transfer 2018;140:1–9. https://doi.org/10.1115/1.4039353.

[29] Agazhanov AS, Samoshkin DA, Kozlovskii YM. Thermophysical properties of Inconel 718 alloy. Journal of Physics: Conference Series 2019;1382. https://doi.org/10.1088/1742-6596/1382/1/012175.

[30] Montgomery C, Beuth J, Sheridan L, Klingbeil N. Process mapping of Inconel 625 in laser powder bed additive manufacturing. Proceedings - 26th Annual International Solid Freeform Fabrication Symposium - An Additive Manufacturing Conference, SFF 2015 2020:1195–204.

[31] Zhou YH, Zhang ZH, Wang YP, Liu G, Zhou SY, Li YL, et al. Selective laser melting of typical metallic materials: An effective process prediction model developed by energy absorption and consumption analysis. Additive Manufacturing 2019;25:204–17. https://doi.org/10.1016/j.addma.2018.10.046.

[32] Qi T, Zhu H, Zeng X, Yin J. Effect of Si content on the cracking behavior of selective laser melted Al7050. Rapid Prototyping Journal 2019;25:1592–600. https://doi.org/10.1108/RPJ-12-2018-0310.

[33] Soderstrom E, Mendez P. Humping mechanisms present in high speed welding. Science and Technology of Welding and Joining 2006;11:572–9. https://doi.org/10.1179/174329306X120787.

[34] Ma XFF, Zhai HLL, Zuo L, Zhang WJJ, Rui SSS, Han QNN, et al. Fatigue short crack propagation behavior of selective laser melted Inconel 718 alloy by in-situ SEM study: Influence of orientation and temperature. International Journal of Fatigue 2020;139:105739. https://doi.org/10.1016/j.ijfatigue.2020.105739.

[35] Zhang D, Niu W, Cao X, Liu Z. Effect of standard heat treatment on the microstructure and mechanical properties of selective laser melting manufactured Inconel 718 superalloy. Materials Science and Engineering A 2015;644:32–40. https://doi.org/10.1016/j.msea.2015.06.021.

[36] Schneider CRA, Maddox SJ. Best practice guide on statistical analysis of fatigue data. Granta Park, Great Abington, Cambridge, UK: 1994.

[37] Vander Voort GF, Manilova EP. Metallographic techniques for superalloys. Microscopy and Microanalysis 2004;10:690–1. https://doi.org/10.1017/S1431927604883442.

[38] Schindelin J, Arganda-Carreras I, Frise E, Kaynig V, Longair M, Pietzsch T, et al. Fiji: an open-source platform for biological-image analysis. Nature Methods 2012;9:676–82. https://doi.org/10.1038/nmeth.2019.

[39] Special Metals. Inconel alloy 718 - SMC-045. 2007.

[40] Solberg K, Berto F. The effect of defects and notches in quasi-static and fatigue loading of Inconel 718 specimens produced by selective laser melting. International Journal of Fatigue 2020;137:105637. https://doi.org/10.1016/j.ijfatigue.2020.105637.

[41] Konečná R, Kunz L, Nicoletto G, Bača A. Long fatigue crack growth in Inconel 718 produced by selective laser melting. International Journal of Fatigue 2016;92:499–506. https://doi.org/10.1016/j.ijfatigue.2016.03.012.

[42] Kaynak Y, Tascioglu E. Post-processing effects on the surface characteristics of Inconel 718 alloy fabricated by selective laser melting additive manufacturing. Progress in Additive Manufacturing 2020;5:221–34. https://doi.org/10.1007/s40964-019-00099-1.

[43] Dowling NE, Calhoun CA, Arcari A. Mean stress effects in stress-life fatigue and the Walker equation. Fatigue and Fracture of Engineering Materials and Structures 2009;32:163–79. https://doi.org/10.1111/j.1460-2695.2008.01322.x.

[44] Walker K. The Effect of Stress Ratio During Crack Propagation and Fatigue for 2024-T3 and 7075-T6 Aluminum. Effects of Environment and Complex Load History on Fatigue Life n.d.:1-1–14. https://doi.org/10.1520/STP32032S.

[45] Mercelis P, Kruth JP. Residual stresses in selective laser sintering and selective laser melting. Rapid Prototyping Journal 2006;12:254–65. https://doi.org/10.1108/13552540610707013.

[46] Moda M, Monelli BD, Benassi M, Palladino M. Validation of a multi-scale simulation strategy based on the Pointwise Strain Superposition Method. IOP Conference Series: Materials Science and Engineering 2021;1038:012022. https://doi.org/10.1088/1757-899x/1038/1/012022.

[47] Wolf E. Fatigue crack closure under cyclic tension. Engineering Fracture Mechanics 1970;2:37–45. https://doi.org/10.1016/0013-7944(70)90028-7.

[48] Rigon D, Meneghetti G. An engineering estimation of fatigue thresholds from a microstructural size and Vickers hardness: application to wrought and additively manufactured metals. International Journal of Fatigue 2020;139:105796. https://doi.org/10.1016/j.ijfatigue.2020.105796.

[49] Rigon D, Meneghetti G. Engineering estimation of the fatigue limit of wrought and defective additively manufactured metals for different load ratios. International Journal of Fatigue 2022;154:106530. https://doi.org/10.1016/j.ijfatigue.2021.106530.

[50] Bertolini R, Campagnolo A, Sorgato M, Ghiotti A, Bruschi S, Meneghetti G. Fatigue strength of LPBF Ti6Al4V machined under flood and cryogenic lubri-cooling conditions. International Journal of Fatigue 2022;162:106973. https://doi.org/10.1016/j.ijfatigue.2022.106973.

[51] Beretta S, Romano S. A comparison of fatigue strength sensitivity to defects for materials manufactured by AM or traditional processes. International Journal of Fatigue 2017;94:178–91. https://doi.org/10.1016/j.ijfatigue.2016.06.020.